

A NEW SPINEL HIGH-ENTROPY OXIDES NANOPARTICLES (FECONIMNZN)₃O₄ AS ANODE
MATERIALS FOR LITHIUM-ION BATTERIES



A Thesis Submitted in Partial Fulfillment of the Requirements
for the Degree of Master of Science in Nanoscience and Technology (Interdisciplinary Program)
Inter-Department of Nanoscience and Technology
GRADUATE SCHOOL
Chulalongkorn University
Academic Year 2022
Copyright of Chulalongkorn University

อนุภาคนาโนออกไซด์เอนโทโรไพสูงแบบสปีเนล (FeCoNiMnZn)₃O₄ เพื่อเป็นวัสดุแอโนดสำหรับ
แบตเตอรี่ลิเทียมไอออน



วิทยานิพนธ์นี้เป็นส่วนหนึ่งของการศึกษาตามหลักสูตรปริญญาวิทยาศาสตรมหาบัณฑิต
สาขาวิชาวิทยาศาสตร์นาโนและเทคโนโลยี (สหสาขาวิชา) สหสาขาวิชาวิทยาศาสตร์นาโนและ
เทคโนโลยี

บัณฑิตวิทยาลัย จุฬาลงกรณ์มหาวิทยาลัย

ปีการศึกษา 2565

ลิขสิทธิ์ของจุฬาลงกรณ์มหาวิทยาลัย

Thesis Title	A NEW SPINEL HIGH-ENTROPY OXIDES NANOPARTICLES ($(\text{FeCoNiMnZn})_3\text{O}_4$) AS ANODE MATERIALS FOR LITHIUM- ION BATTERIES
By	Miss Maha Nur Aida
Field of Study	Nanoscience and Technology (Interdisciplinary Program)
Thesis Advisor	NUMPON INSIN
Thesis Co Advisor	JIAQIAN QIN

Accepted by the GRADUATE SCHOOL, Chulalongkorn University in Partial
Fulfillment of the Requirement for the Master of Science

..... Dean of the GRADUATE SCHOOL
(YOOTTHANA CHUPPUNNARAT)

THESIS COMMITTEE

..... Chairman
(RATTHAPOL RANGKUPAN)

..... Thesis Advisor
(NUMPON INSIN)

..... Thesis Co-Advisor
(JIAQIAN QIN)

..... Examiner
(NIPAKA SUKPIROM)

..... External Examiner
(Tosapol Maluangnont)

มาฮา นูร์ ไอดา : อนุภาคนาโนออกไซด์เอนโทรปีสูงแบบสปินเนล (FeCoNiMnZn)₃O₄ เพื่อเป็นวัสดุแอโนดสำหรับแบตเตอรี่ลิเทียมไอออน. (A NEW SPINEL HIGH-ENTROPY OXIDES NANOPARTICLES (FECONIMNZN)₃O₄ AS ANODE MATERIALS FOR LITHIUM-ION BATTERIES) อ.ที่ปรึกษาหลัก : นำพล อินสิน, อ.ที่ปรึกษาร่วม : เจีย เซียน ฉิน

วัสดุออกไซด์เอนโทรปีสูง (FeCoNiMnZn)₃O₄ สำหรับเป็นขั้วแอโนดในแบตเตอรี่ชนิดลิเทียมไอออนได้ถูกสังเคราะห์ขึ้นเป็นครั้งแรกด้วยกระบวนการไฮโดรเทอร์มอล โดยได้สังเคราะห์ออกไซด์ของโลหะเดี่ยวที่เป็นองค์ประกอบของออกไซด์เอนโทรปีสูงแต่ละชนิด ได้แก่ เหล็ก, โคบอลต์, นิกเกิล, แมงกานีส และสังกะสี ด้วยวิธีเดียวกันเพื่อใช้เปรียบเทียบ สารตัวอย่างได้ถูกพิสูจน์เอกลักษณ์ด้วยเทคนิคการเลี้ยวเบนของรังสีเอกซ์, กล้องจุลทรรศน์อิเล็กตรอนแบบส่องกราด, กล้องจุลทรรศน์อิเล็กตรอนแบบส่องผ่าน, การสร้างแผนที่การกระจายของธาตุจากสัญญาณฟลูออเรสเซนซ์ของรังสีเอกซ์, การวิเคราะห์พื้นผิว, inductively-coupled plasma-optical emission spectroscopy และ X-ray photoelectron spectroscopy สมรรถนะทางเคมีไฟฟ้าของวัสดุที่ได้ ผ่าน การ ศึกษา โดย Cyclic voltammetry, galvanostatic charge-discharge, electrochemical impedance spectroscopy, และ associated coulombic efficiencies สารตัวอย่าง 3 ชนิด ได้แก่ HEO-3, HEO-6, และ HEO-9 ซึ่งได้จากการเปลี่ยนแปลงอุณหภูมิในการสังเคราะห์ได้ถูกนำมาศึกษา โดยอนุภาค HEO-3 เป็นอนุภาคที่มีขนาดเล็กที่สุด โดยมีเส้นผ่านศูนย์กลาง 2.95 ± 0.29 นาโนเมตรและมีรูปร่างไม่สม่ำเสมอ ในขณะที่ อนุภาค HEO-6 และ HEO-9 มีขนาดเส้นผ่านศูนย์กลาง 23.16 ± 7.56 นาโนเมตร และ 90.42 ± 3.27 นาโนเมตร ตามลำดับ HEO-9 แสดงสมบัติทางเคมีไฟฟ้าที่ดี โดยมีประสิทธิภาพในการเก็บประจุ $625.5 \text{ mA h g}^{-1}$ ที่ 1000 mA g^{-1} และมีความจุ $1333.54 \text{ mA h g}^{-1}$ ที่ 50 mA g^{-1} หลังจากการใช้งาน การเปลี่ยนแปลงทางกายภาพและทางเคมีของวัสดุได้ถูกตรวจสอบ โดยพบว่า HEO-9 มีสมรรถนะที่คงที่มากที่สุดและมีการเปลี่ยนแปลงทางปริมาตรน้อยที่สุด จากผลการทดลอง การพัฒนาขั้วแอโนดโดยใช้วัสดุออกไซด์เอนโทรปีสูงนี้มีศักยภาพที่ดีในการพัฒนาต่อไป.

สาขาวิชา	วิทยาศาสตร์นาโนและ เทคโนโลยี (สหสาขาวิชา)	ลายมือชื่อนิสิต
ปีการศึกษา	2565	ลายมือชื่อ อ.ที่ปรึกษาหลัก
		ลายมือชื่อ อ.ที่ปรึกษาร่วม

6488068620 : MAJOR NANOSCIENCE AND TECHNOLOGY (INTERDISCIPLINARY PROGRAM)

KEYWORD: high-entropy oxides nanoparticles anode lithium-ion batteries

Maha Nur Aida : A NEW SPINEL HIGH-ENTROPY OXIDES NANOPARTICLES (FECONIMNZN)₃O₄ AS ANODE MATERIALS FOR LITHIUM-ION BATTERIES.

Advisor: NUMPON INSIN Co-advisor: JIAQIAN QIN

A novel (FeCoNiMnZn)₃O₄ HEO as an anode in lithium-ion batteries (LIBs) was developed for the first time. High-entropy oxide (HEO) of (FeCoNiMnZn)₃O₄ was synthesized using a hydrothermal technique to control size and crystallinity. We also synthesized oxides of each element (Fe, Co, Ni, Mn, Zn) from HEO composition under similar condition for comparison. The samples were then analyzed using XRD, SEM, TEM, EDS elemental mapping, surface area analysis, ICP-OES, and XPS. Cyclic voltammetry, galvanostatic charge-discharge, electrochemical impedance spectroscopy, and associated coulombic efficiencies were also used to study the electrochemical performance of (FeCoNiMnZn)₃O₄. Three samples with different preparation conditions, HEO-3, HEO-6, and HEO-9, were selected for investigation. HEO-3 particles are the smallest, 2.95 ± 0.29 nm, and have an irregular shape, making them difficult to measure. In contrast, HEO-6 and HEO-9 particles have diameters between 23.16 ± 7.56 nm and 90.42 ± 3.27 nm, respectively. The HEO-9 performs exceptionally well electrochemically. It exhibits excellent performance of $625.5 \text{ mA h g}^{-1}$ at 1000 mA g^{-1} and a large capacity of $1333.54 \text{ mA h g}^{-1}$ at 50 mA g^{-1} . After cycling, we also investigated the physical and chemical characterization to identify the change. HEO-9 still has a more stable performance and the least volume change. From these results, developing an anode for lithium-ion batteries (LIBs) in the future looks promising.

Field of Study: Nanoscience and
Technology

(Interdisciplinary Program)

Academic Year: 2022

Student's Signature

Advisor's Signature

Co-advisor's Signature

ACKNOWLEDGEMENTS

Firstly, I would like to express my sincere gratitude to Assistant Professor Dr. Numpon Insin, who is the advisor of my thesis, and Dr. Jiaqian Qin, who is the co-advisor of my thesis, for their ongoing support of my Master of Science (M.Sc.) study and research, and for consistently and convincingly conveying an excitement for teaching and a spirit of adventure regarding research. The coaching was helpful throughout my entire research and thesis writing period. This thesis would not have been possible without the suggestions and constant aid. Along with my advisor, I aspire to extend my sincere gratitude to the other members of my thesis committee, Assistant Professor Dr. Rattapol Rangkupan, Assistant Professor Dr. Nipaka Sukpirom, and Associate Professor Tosapol Maluangnont, for sharing their advice and assistance with me throughout the writing of my thesis, as well as for their inspiration and insightful criticism.

The Graduate Scholarship Programme for ASEAN or Non-ASEAN Countries at Chulalongkorn University is also greatly appreciated for allowing me to pursue my M.Sc. The other particular group to whom I want to express my deepest thanks is my family, who have given me all I have ever needed, and my friends, who have always been there to support and love me. Additionally, I thank all the members of NI's and Qin's groups who assisted me with their kind assistance, friendliness, and encouragement. I am thankful as a human, a child, ARMY, ELF, EXO-L, NCTzen, and CARAT have stayed up through finishing this thesis.

Maha Nur Aida

TABLE OF CONTENTS

	Page
ABSTRACT (THAI).....	iii
ABSTRACT (ENGLISH).....	iv
ACKNOWLEDGEMENTS.....	v
TABLE OF CONTENTS.....	vi
LIST OF TABLES.....	ix
LIST OF FIGURES.....	xi
CHAPTER 1.....	1
INTRODUCTION.....	1
1.1 Rational.....	1
1.2 Objectives.....	1
1.3 Expected beneficial outcome.....	2
CHAPTER 2.....	3
THEORY AND LITERATURE REVIEWS.....	3
2.1 Lithium-ion batteries (LIBs).....	3
2.1.1 Components.....	3
2.1.2 Scheme of lithium-ion batteries.....	4
2.1.3 Materials for Anodes.....	7
2.2 High-entropy oxides.....	8
2.2.1 Configurational entropy.....	8
2.2.2 Lithium-ion battery research on HEO anode materials.....	10
CHAPTER 3.....	12

METHODOLOGY.....	12
3.1 Material synthesis.....	12
3.2 Electrode Preparation and cell assembly.....	13
3.3 Characterizations of the Materials and Electrochemistry.....	15
CHAPTER 4.....	16
RESULTS AND DISCUSSION.....	16
4.1 Structures and morphologies of $(\text{FeCoNiMnZn})_3\text{O}_4$	16
4.1.1 X-ray Diffraction (XRD).....	16
4.1.2 X-ray photoelectron spectroscopy (XPS).....	29
4.1.3 Scanning Electron Microscope (SEM).....	33
4.1.4 Energy dispersive X-ray spectroscopy (EDS).....	35
4.1.5 Inductively coupled plasma optical emission spectroscopy (ICP-OES).....	42
4.1.6 Transmission Electron Microscope (TEM).....	46
4.1.7 BET Surface area analysis.....	46
4.2 Electrochemical performance of $(\text{FeCoNiMnZn})_3\text{O}_4$	49
4.2.1 Cyclic voltammetry (CV).....	49
4.2.2 Galvanostatic charge-discharge.....	52
4.2.3 Cycling performance, the coulombic efficiencies, and rate capability.....	57
4.2.4 Electrochemical impedance spectroscopy (EIS).....	62
4.3 After cycling performance of $(\text{FeCoNiMnZn})_3\text{O}_4$	64
4.3.1 X-ray Diffraction (XRD) after cycling performances.....	64
4.3.2 Scanning Electron Microscope (SEM) and Energy dispersive X-ray spectroscopy (EDS) after cycling performances.....	67
4.3.3 ICP-OES after cycling performances.....	72

CHAPTER 5.....	77
CONCLUSION	77
5.1 Conclusion	77
5.2 Recommendations for future work	77
REFERENCES	79
VITA.....	88



LIST OF TABLES

Table 1. The anode material in the previous work.....	8
Table 2. The detail information about rhodochrosite crystal structure.	21
Table 3. The detail information about magnetite crystal structure.	22
Table 4. Summary of each metal oxide of Fe, Co, Ni, Mn, Zn, and HEO.	24
Table 5. The detail information about hematite crystal structure.	24
Table 6. The detail information about Cobalt dicobalt (III) oxide crystal structure.	25
Table 7. The detail information about nickel oxides crystal structure.	27
Table 8. The detail information about bixbyite crystal structure.	28
Table 9. The detail information about Zinc oxide crystal structure.....	29
Table 10. Elemental percentages of $(\text{FeCoNiMnZn})_3\text{O}_4$ at 300°C	377
Table 11. Elemental percentages of $(\text{FeCoNiMnZn})_3\text{O}_4$ at 600°C	377
Table 12. Elemental percentages of $(\text{FeCoNiMnZn})_3\text{O}_4$ at 900°C	38
Table 13. Elemental percentages of each basic oxide.....	38
Table 14. ICP-OES concentration and corresponding calculated entropy configuration values of the obtained samples.....	433
Table 15. The current setting on the instrument.	53
Table 16. The specific capacity of Ni, Mn, Co, Fe, HEO-3, HEO-6, and HEO-9 oxides at 100 mA g^{-1}	55
Table 17. The specific capacity of HEO-3, HEO-6, and HEO-9 at different current conditions.....	56
Table 18. HEO-3, HEO-6, and HEO-9's specific capacity at cycles 1, 10, 30, and 50 at 500 mA g^{-1}	59
Table 19. The specific capacity of each elemental oxide at cycles 1, 10, 30, and 50 at 100 mA g^{-1}	60
Table 20. The specific capacity of HEO-9 at cycles 1, 5, 10, 25, 50, and 100 at 1.0 A g^{-1}	60
Table 21. Summary of lithium storage properties of HEO.	60
Table 22. The specific capacity of HEO-3, HEO-6, and HEO-9 at different conditions.	61
Table 23. The fitted kinetic parameters of HEO.....	62

Table 24. The elemental concentration of HEO-9 was examined using EDS after 50 cycles.	70
Table 25. Elemental distribution of HEO-9 after 50 cycles by ICP-OES measurement.	74



LIST OF FIGURES

Fig. 1. The lithium-ion battery's component (LIBs).....	3
Fig. 2. The detailed scheme of a lithium-ion battery [36].	5
Fig. 3. Electrochemical reactions that occur during charging.	5
Fig. 4. Electrochemical reactions during discharge.	6
Fig. 5. Alloy types based on configurational entropy [50].	9
Fig. 6. The reaction scheme for the hydrothermal method.....	13
Fig. 7. Products from different calcination conditions a) as-synthesized and after three different temperatures at b) 300°C, c) 600°C, and d) 900°C.	13
Fig. 8. As-synthesized appearance of a) Fe, b) Co, c) Ni, d) Mn, and e) Zn oxides.	13
Fig. 9. Electrode preparation using $(\text{FeCoNiMnZn})_3\text{O}_4$	14
Fig. 10. The steps of cell assembly $(\text{FeCoNiMnZn})_3\text{O}_4$	14
Fig. 11. The sequences of coin cells.....	15
Fig. 12. XRD patterns of HEO-NP at different temperatures and as-synthesized.	20
Fig. 13. Unit cell of rhodochrosite crystal structure.	21
Fig. 14. a) Unit cell of the spinel structure, b) in a polyhedral form where red (oxygen); green (tetrahedral site); blue (octahedral site), c) a schematic illustration of the structure of HEO, d) view along an axis, the figure of octahedral site e) and tetrahedral side f).....	22
Fig. 15. XRD patterns of a) Iron oxide in comparison with reference (PDF#00-033-0664), b) Cobalt oxide in comparison with reference (PDF#01-080-1533), c) Nickel in comparison with reference (PDF#01-078-4374), d) Manganese in comparison with reference (PDF#01-089-2809), and e) Zinc in comparison with reference (PDF#01-080-0075).....	23
Fig. 16. Unit cell of hematite crystal structure.	24
Fig. 17. Unit cell of Cobalt dicobalt (III) oxide crystal structure.....	25
Fig. 18. Unit cell of nickel oxide crystal structure.	26
Fig. 19. Unit cell of bixbyite crystal structure.	27
Fig. 20. Unit cell of zinc oxide crystal structure.	28
Fig. 21. The reaction of urea hydrolysis.	30

Fig. 22. XPS images of HEO-6 (a) Fe 2p, (b) Co 2p, (c) Ni 2p, (d) Mn 2p, (e) Zn 2p, and (f) O 1s spectra.....	31
Fig. 23. XPS images of HEO-9 (a) Fe 2p, (b) Co 2p, (c) Ni 2p, (d) Mn 2p, (e) Zn 2p, and (f) O 1s spectra.....	32
Fig. 24. XPS complete spectroscopy of HEO-9.....	32
Fig. 25. SEM images and histograms of the particle size distribution of a) HEO-3, b) HEO-6, and c) HEO-9.	34
Fig. 26. SEM image and histogram of particle size of a) Fe, b) Co, c) Ni, d) Mn, and e) Zn oxides.....	34
Fig. 27. The distribution of diameter of each elemental and high-entropy oxide.....	35
Fig. 28. EDS elemental mapping images of $(\text{FeCoNiMnZn})_3\text{O}_4$ at 300°C	39
Fig. 29. EDS elemental mapping images of $(\text{FeCoNiMnZn})_3\text{O}_4$ at 600°C	40
Fig. 30. EDS elemental mapping images of $(\text{FeCoNiMnZn})_3\text{O}_4$ at 900°C	41
Fig. 31. TEM images of $(\text{FeCoNiMnZn})_3\text{O}_4$ at a) HEO-3, b) HEO-6, and c) HEO-9.....	46
Fig. 32. N ₂ adsorption–desorption isotherms of HEO-3, HEO-6, and HEO-9 samples. ..	47
Fig. 33. CV curves for a) HEO-3, b) HEO-6, and c) HEO-9 at 0.1 mVs^{-1} and $0.00 - 3.00 \text{ V}$	50
Fig. 34. CV curves of $(\text{FeCoNiMnZn})_3\text{O}_4$ a) HEO-3, b) HEO-6, c) HEO-9 at different scan rates $0.1 - 1.0 \text{ mV/s}$	51
Fig. 35. The initial CV curves for a) Fe, b) Co, c) Ni, and d) Zn oxides at 0.1 mV/s	52
Fig. 36. The formula of specific capacitance.....	52
Fig. 37. Initial five charge & discharge curves of a) NiO, b) Mn_2O_3 , c) Co_3O_4 , d) Fe_2O_3 , e) HEO-3, f) HEO-6, and g) HEO-9 electrodes calculated at 100 mA g^{-1}	55
Fig. 38. Charge & discharge curves of the HEO-3, HEO-6, and HEO-9, measured at different specific currents a), b), and c), respectively.	56
Fig. 39. a) Evaluation of cycling stability of several HEO electrodes at 500 mA g^{-1} for 50 cycles, b) the performance for 50 cycles of Iron, Cobalt, Nickel, and Zinc oxides at 100 mA/g , c) The performances 100 cycles scan rates at 1.0 A/g , and d) the different cycles of charge-discharge curves at 1000 mA/g of HEO-9.	59
Fig. 40. The ability of different HEO electrodes to compare rates.	61
Fig. 41. EIS Nyquist plots of various HEO electrodes.	62

Fig. 42. XRD comparison patterns as-synthesized, electrode and after 50 cycles of a) HEO-3, b) HEO-6, and c) HEO-9.....	66
Fig. 43. XRD patterns of comparison as-synthesized and electrode oxides of a) Fe, b) Co, c) Ni, d) Mn, and e) Zn.	66
Fig. 44. XRD patterns after 50 cycles of Iron, Cobalt, Nickel, and Manganese oxides.	67
Fig. 45. XRD pattern at different charges a), Morphology characterization of electrodes. Cross-sectional SEM images of the electrode before b) HEO-3, c) HEO-6, d) HEO-9. Cross-sectional SEM images of the electrode after 50 cycles e) HEO-3, f) HEO-6, g) HEO-9. EDS elemental mapping of HEO-9 after 50charge–discharge cycles h).....	69



CHAPTER 1

INTRODUCTION

1.1 Rational

Lithium-ion batteries (LIBs) are widely used because they have a high energy density, sizeable specific capacity, environment-friendly practices, and longer charge retention [1]. Graphite is typically made up of commercials in the market because of its low working potential, low cost, and good cycle life. However, it has a lower theoretical capacity, merely 372 mAh g^{-1} [2-7]. By the battery structure, improving the electrode materials is necessary for enhancing the performance of LIBs [8] to get a higher capacity, and many researchers used elemental anodes (such as Si, P, Sb) and transition-metal oxides (TMOs) [9, 10]. Iron (Fe_2O_3 and Fe_3O_4), nickel (NiO), and manganese oxides (Mn_3O_4 and MnO_2) were used as anode materials because of non-toxicity, high abundance, low cost, improved safety, and non-flammable nature; meanwhile, cobalt oxides (CoO) and zinc oxide (ZnO) were used because of high theoretical Li-ion storage capacities [11-19]. Unfortunately, metal oxide anodes suffer from significant volume change and low ionic conductivity, making them inferior to cycling stability and poor rate performance [20].

Recently, high entropy oxides (HEO), a new class of materials usually containing five or more mixed oxides, demonstrated unique, desirable physical and chemical properties in a single-phase oxide system with effective stabilization entropy. High entropy oxides attract significant attention among various anode candidates because of their capacities between 500 and 1000 mAh g^{-1} [21]. They can be long cycled without considerable capacity degradation, so it is promising for better performance since they can bring more significant capacity, rate capability, and cycling process [22]. In this work, HEO containing Fe, Co, Ni, Mn, and Zn will be synthesized and investigated for their performance as anodes in LIBs.

1.2 Objectives

1. To synthesize and characterize the physical properties of new high entropy oxides
2. To investigate the electrochemical performance of the materials

3. To evaluate the material as electrodes for lithium-ion batteries

1.3 Expected beneficial outcome

With outstanding performance, high-entropy oxide nanoparticles $(\text{FeCoNiMnZn})_3\text{O}_4$ can be produced hydrothermally as a novel anode material for lithium-ion batteries.



CHAPTER 2

THEORY AND LITERATURE REVIEWS

2.1 Lithium-ion batteries (LIBs)

2.1.1 Components

A lithium-ion battery (LIBs) is a category of rechargeable batteries that utilizes lithium ions as a critical element of its electrochemistry. During charging and discharging, these ions flow between the negative (anode) and positive (cathode) electrodes [23]. The cathode, anode, electrolyte, and separator are the four parts that makeup Li-ion batteries (LIBs) (Fig. 1). Each unit plays a significant role in its function [24]. The cathode is highly necessary for lithium-ion batteries because it is a reduction that wants to gain electrons. At the same time, the anode has the function of giving the electrons as oxidation. Furthermore, electrolytes are the main component between both electrodes, which can make a battery conductive. Next, a separator is a part that prevents physical contact between the electrodes [25]. The invention of LIBs by John B. Goodenough, M. Stanley Whittingham and Akira Yoshino had given the improvement almost twice Ni-Cd because the performance, such as exceptional life of a cycle, safety, and speedy charging, is better [26].

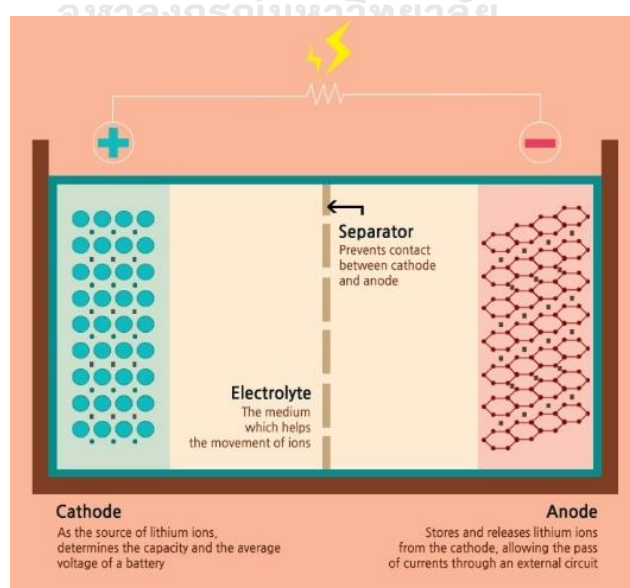


Fig. 1. The lithium-ion battery's component (LIBs).

LIBs are one type of battery widely used as an energy source [27]. Due to its high energy density, lightweight, and numerous uses, this type of battery has been employed in a wide range of devices, including mobile phones, digital cameras, laptops, and even robots and automobiles [28], then giving the high capacity's rate and stabilization of cycling [29]. Moreover, LIBs offer many advantages, such as longer life cycles, soft self-discharge, and no memory of effect [30]. Lithium-ion batteries produce the highest voltage, three times higher than other batteries, compared to lead acid, nickel-metal hydride (Ni-MH), nickel-cadmium (Ni-Cd), and lithium-ion batteries. These batteries use both electrodes' redox reactions (reduction and oxidation) to generate electricity [31]. LIBs have other uses, such as enhancing the kinetic performance and promoting the catalytic through biomass pyrolysis or gasification [32].

2.1.2 Scheme of lithium-ion batteries

Lithium-ion batteries are often known as rechargeable batteries [33], and both reduction and oxidation reactions occur when an electric charge is applied and removed [34]. Before using a lithium battery, it is usually necessary to charge it, which moves the flow of electrons from the voltage source from the cathode to the anode. Equilibrium is established when lithium ions at the cathode migrate through the electrolyte and separator toward the anode pole, signaling that the battery is fully charged [35]. The reverse happens when lithium batteries are utilized. Then, a flow of electrons carrying an electric charge occurs via the load from the anode pole to the cathode pole. Lithium ions from the anode pole move to the cathode pole during this movement, as depicted in Fig. 2, passing through the electrolyte and entering the pores of the separator [36]. The anode reaction is the process through which the anode provides electrons to the external circuit after discharge. On the other hand, as it is charging, a process known as the cathode reaction occurs in which it takes electrons from the external circuit. Fig. 3-4 shows the electrochemical response during charging and discharging for a more thorough understanding.

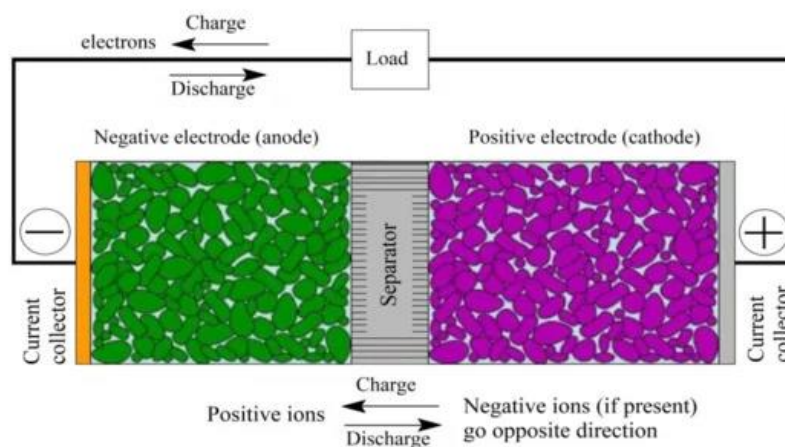


Fig. 2. The detailed scheme of a lithium-ion battery [36].

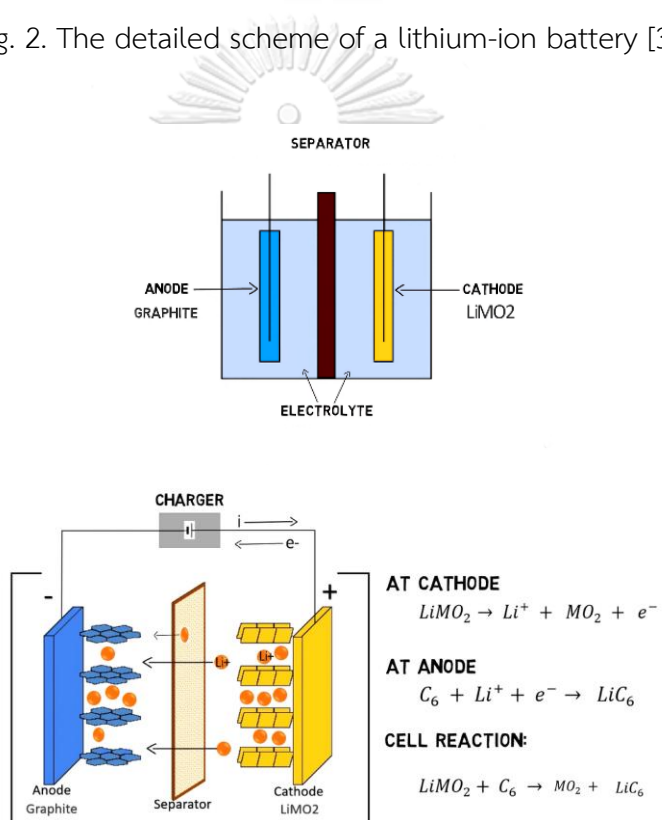


Fig. 3. Electrochemical reactions that occur during charging.

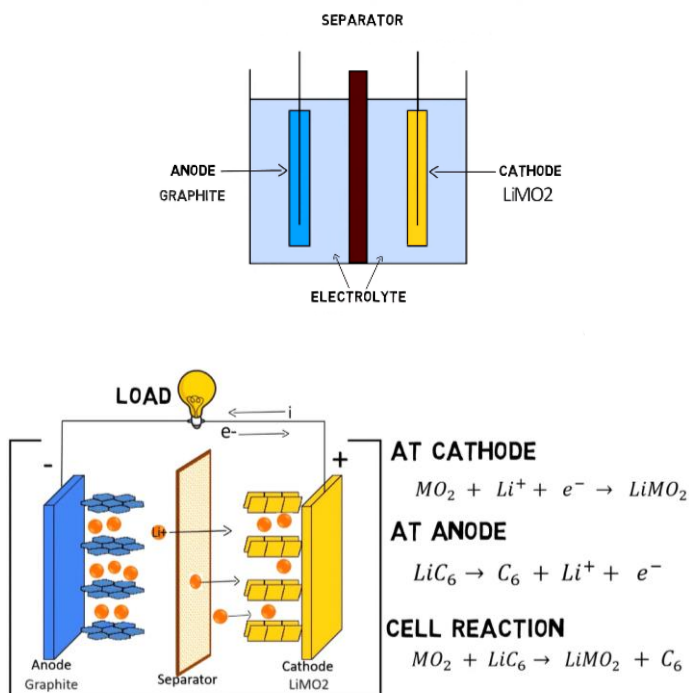


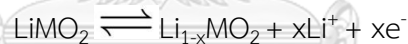
Fig. 4. Electrochemical reactions during discharge.

Following this reaction, the resume can be seen below:

Positive electrode

M: transition metal

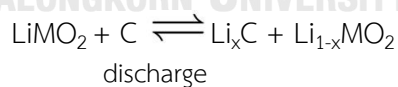
charge



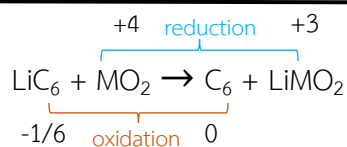
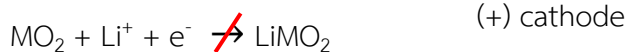
Negative electrode



Overall reaction



Discharge lithium-ion



2.1.3 Materials for Anodes

In lithium-ion batteries, the anode is one of the two electrodes, the other being the cathode. The anode in a lithium-ion battery is typically made of carbon-based materials, such as graphite, that can intercalate lithium ions during the battery's charging process. Here are the characteristics of the anode:

- 1) **Lithium Host:** The anode serves as a host for lithium ions during the charging and discharging processes. It allows for the reversible insertion and extraction of lithium ions as the battery charges and discharges.
- 2) **Electron Conductor:** The anode material should have good electron conductivity to enable the flow of electrons between the anode and the external circuit during charge and discharge.

The desired properties of the anode:

- 1) **High Lithium Storage Capacity:** The anode should possess a high capacity for storing and releasing lithium ions. This capacity directly affects the battery's overall energy storage capacity and runtime.
- 2) **Stability and Cyclability:** The anode material should be chemically stable and capable of withstanding numerous charge and discharge cycles without significant degradation. This property ensures the long-term performance and durability of the battery.
- 3) **Low Potential for Side Reactions:** The anode should have a common tendency for unwanted side reactions with the electrolyte, which could cause capacity loss, decreased efficiency, or safety hazards.
- 4) **Mechanical Strength:** The anode material should be mechanically robust to withstand the stress and strain of repeated charge and discharge cycles. This property helps prevent structural damage, cracking, or loss of electrical contact within the electrode.
- 5) **Compatibility with Other Battery Components:** The anode material should be compatible with the other components of the battery, including the cathode and electrolyte. Compatibility ensures the overall battery system's optimal performance, stability, and safety.

Working Principle:

During charging: When the battery is being charged, lithium ions are extracted from the cathode material (typically a metal oxide) and move through the electrolyte towards the anode. During discharging: The process is reversed when the battery is discharged. The stored lithium ions in the anode move back through the electrolyte to the cathode, releasing their stored energy and enabling the battery to power external devices.

There are some previous works (Table 1) about the materials for anodes starting with graphite first and continuing to change to metal oxides due to some reasons.

Table 1. The anode material in the previous work.

Anode		Benefits	Drawbacks
Graphite		Long cycle life	Limited capacity (372 mAh/g)
		High Capacity	Poor rate capability
		Acceptable cost	
Metal oxides	Fe ₂ O ₃ ; Fe ₃ O ₄	Non-flammable	Suffer large volume change & low ionic conductivity
	NiO	High abundance	
	Mn ₃ O ₄ ; MnO ₂	Non-toxicity	
	CoO	High Capacity	
	ZnO	Improved cyclability	

2.2 High-entropy oxides

2.2.1 Configurational entropy

Since 2004, high-entropy alloys (HEAs), which mix several metals to create innovative components with five or more elements [37], have been used to provide the balance of properties in multicomponent alloy systems [38]. Due to their single-phase structure, these materials exhibit a unique combination of disordering and

crystal periodicity [39]. Because of its purpose and potential applications over conventional research, many scientists tried to conduct it for a long time [40]. High Entropy Alloys (HEAs) offer strength-ductility synergy [41], great electrocatalysts [42], supercapacitors [43, 44], and rechargeable batteries [45]. Furthermore, high-entropy nitride was the first to be made available in 2005. High entropy oxides, high-entropy metal diborides, high entropy carbides, high entropy sulfides, high entropy fluorides, and high entropy alumino-silicides then followed it. Numerous high entropy compounds that have been successfully employed in various kinds of complex materials have been studied by HEAs [46].

Oxides with five or more components in a single-phase oxide system and configurational entropy (S_{config}) larger than $1.5R$ are referred to as high-entropy oxides (HEO) (R is the universal gas constant) [47]. Rost *et al.* performed HEO for the first time with efficient stabilization entropy in 2015 utilizing equimolar quantities of five oxides, MgO, NiO, CuO, CoO, and ZnO, in a rock salt structure. A greater entropy value could provide excellent functional qualities due to high configurational entropy, which has three different forms in Fig. 5 [48]. Additionally, HEO exhibits a high Li-ion conductivity ($>10^{-3} \text{ S cm}^{-1}$), which is more than two orders of magnitude better than that of LiPON (lithium phosphorous oxy-nitride) solid electrolyte (whose ionic conductivity at 25°C is around $2 \times 10^{-6} \text{ S cm}^{-1}$) among the greatest ever reported in oxides [49]. As a result, there are many potential applications for this novel family of materials.

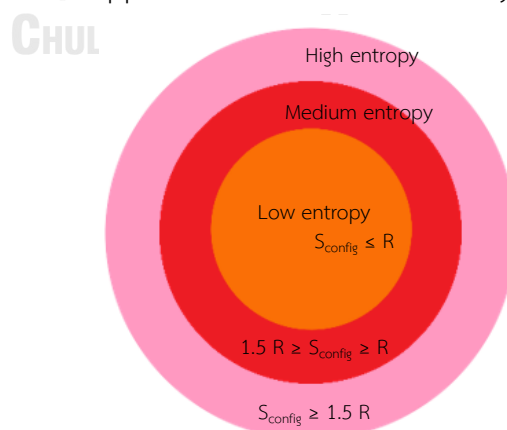


Fig. 5. Alloy types based on configurational entropy [50].

Corresponding to the Boltzmann equation, illustrated in Equation (1), the increased number of elements often results in higher configuration entropy ($S_{\text{config}} = 1.5R$) to establish a single-phase solid solution structure. This is the fundamental idea behind high-entropy oxides. Corresponding to thermodynamic formula (2), if ΔH_{mix} is constant, the system's stability will be enhanced by the decreased free energy ΔG_{mix} resulting from the increased mixing entropy ΔS_{mix} . This is one method for improving HEO's electrochemical performance. The following formula was used to get the configurational entropy:

$$S_{\text{config}} = -R \left[\left(\sum_{i=1}^N x_i \ln x_i \right)_{\text{cation-site}} + \left(\sum_{j=1}^N x_j \ln x_j \right)_{\text{anion-site}} \right] \quad (1)$$

$$\Delta G_{\text{mix}} = \Delta H_{\text{mix}} - T\Delta S_{\text{mix}} \quad (2)$$

R equals [8.314 J/mol K] N is the component's number.

R is the gas constant, while x_i and x_j are the mole fractions of ions in the cation and anion sites, respectively. According to earlier studies, a high configurational entropy can help stabilize the lattice. A slow diffusion effect can reduce the self-aggregation of active materials in the anode during lithiation and delithiation, leading to superior cycling performance.

2.2.2 Lithium-ion battery research on HEO anode materials

HEO as anode materials for LIBs was initially described by Sarkar in 2018, and high configurational entropy can offer significant advantages for storage capacity retention and considerably enhance cycling stability. They used the nebulized spray pyrolysis (NSP) method to test (CoCuMgNiZn)O for reversible energy, which is quite encouraging. The same compound with solid-state synthesis as anode material was done by Qiu *et al.* However, there are many challenges and unknown parameters when considering the variety of metal cations and numerous synthesis methods for exceptional performance. Additionally, it has been claimed that high-entropy oxide nanoparticles perform better due to nanomaterials' ability to boost LIBs' electrode rate capabilities by shortening the diffusion length and advancing an area from an electrode

to an electrode-electrolyte [51]. Kheradmandfard has analyzed (MgCuNiCoZn)O nanoparticles made via ultrafast green microwave-assisted synthesis for the first time. One thousand cycles at 1 A/g were used to demonstrate the HEO nanoparticles' outstanding stability [52]. Then, Nguyen *et al.* successfully prepared high entropy spinel oxide, (CrMnFeNiCu)₃O₄, for excellent performance in LIBs using the hydrothermal method, followed by three different calculations at temperatures to offer a convenient way of controlling the particle size and crystallinity. Shape and crystallinity are crucial for achieving the necessary rate capability and cycle performance.

By modifying the constituent elements of HEO, their concentrations, and crystal structures, it is possible to realize an infinite number of different or even novel functional qualities, which has proven challenging for many studies to identify the best potential. *Firstly*, (CoCuMgNiZn) and (FeCoNiCrMn) have been the most studied as anode materials for electrochemical performance because Co, Ni, and Mn are better safety compounds in oxides [53]. *Second*, it was discovered that Zn exhibited superior rate performance, cycle stability, and the highest rate possible given the discharge-specific in (FeNiCrMnX)₃O₄ (X = Zn, Mg) and (FeCoNiCrMnXLi)₃O₄ (X = Cu, Mg, Zn). *Third*, (CoNiZnXMnLi)₃O₄ (X=Fe, Cr) was studied, and it was revealed that Fe could lead to a higher specific capacity. Thus, (FeCoNiMnZn)₃O₄ was selected in our study, considering those factors. The spinel crystal structure of (FeCoNiMnZn)₃O₄ offers a combination of structural stability, thermal stability, high energy density, and fast charge/discharge rates, making it advantageous for various applications, particularly in energy storage and conversion. It will be the first time a new spinel high-entropy oxides nanoparticles will be utilized as anode for LIBs using a hydrothermal process.

CHAPTER 3

METHODOLOGY

3.1 Material synthesis

All chemicals, reagents, and solvents were used without further purification. Iron (III) nitrate nonahydrate ($\text{Fe}(\text{NO}_3)_3 \cdot 9\text{H}_2\text{O}$, Sigma-Aldrich, 98%), cobalt (II) nitrate hexahydrate ($\text{Co}(\text{NO}_3)_2 \cdot 6\text{H}_2\text{O}$, Sigma-Aldrich), nickel (II) nitrate hexahydrate ($\text{Ni}(\text{NO}_3)_2 \cdot 6\text{H}_2\text{O}$, Sigma-Aldrich, 99%), manganese (II) nitrate tetrahydrate ($\text{Mn}(\text{NO}_3)_2 \cdot 4\text{H}_2\text{O}$, Sigma-Aldrich, 97%), zinc nitrate hexahydrate ($\text{Zn}(\text{NO}_3)_2 \cdot 6\text{H}_2\text{O}$, Sigma-Aldrich, 98%), hexadecyltrimethylammonium bromide (CTAB, Sigma-Aldrich, 98%), and urea (Sigma-Aldrich, 99%) were used as purchased.

Hydrothermal methods can help shape materials into small sizes. The addition of some surfactants can control the morphology, size, and phase structure. 20 mL of deionized (DI) water was used to dissolve equal amounts of $\text{Fe}(\text{NO}_3)_3 \cdot 9\text{H}_2\text{O}$, $\text{Co}(\text{NO}_3)_2 \cdot 6\text{H}_2\text{O}$, $\text{Ni}(\text{NO}_3)_2 \cdot 6\text{H}_2\text{O}$, $\text{Mn}(\text{NO}_3)_2 \cdot 4\text{H}_2\text{O}$, and $\text{Zn}(\text{NO}_3)_2 \cdot 6\text{H}_2\text{O}$. The surfactant was subsequently added, CTAB (0.625 mmol). The mixture was stirred to generate a homogenous solution before adding urea (15 mmol). Into 100-mL reaction containers, the obtained solution was put. The hydrothermal procedure took place for 5h at 140 °C. Centrifugation, two rounds of washing with ethanol and DI water, filtration, and overnight drying at 100°C were used to remove the powders from the autoclave. The resulting samples were then annealed in the air for 6h at varied temperatures with a 5°C min⁻¹ ramp as specifically in Fig. 6. The calcination condition displays in Fig. 7 the as-synthesized and three different conditions. They seem to exhibit the same physical properties. Also, as-synthesized basic metal oxides can be seen in Fig. 8.

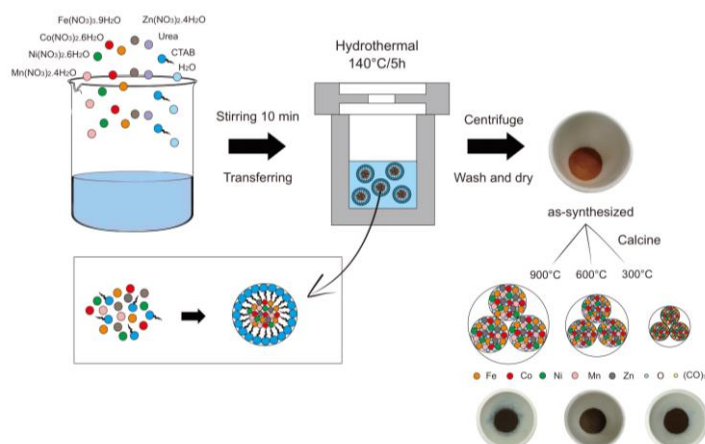


Fig. 6. The reaction scheme for the hydrothermal method.

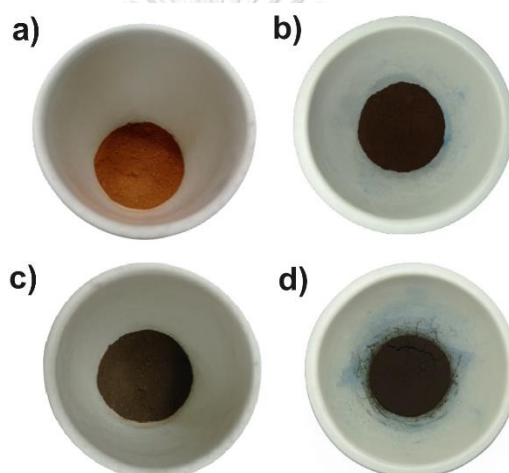


Fig. 7. Products from different calcination conditions a) as-synthesized and after three different temperatures at b) 300°C, c) 600°C, and d) 900°C.

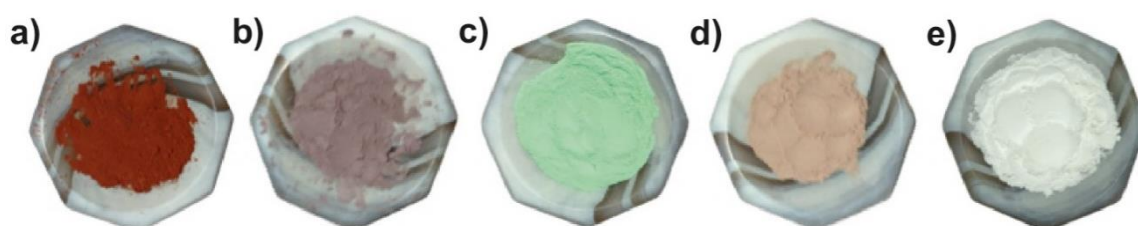


Fig. 8. As-synthesized appearance of a) Fe, b) Co, c) Ni, d) Mn, and e) Zn oxides.

3.2 Electrode Preparation and cell assembly

The electrodes were made by creating a slurry by combining the HEO powder (80 weight percent), acetylene black (10 weight percent), and poly (vinylidene fluoride)

binder (10 weight percent) in N-methyl-2-pyrrolidone (NMP). The slurry was then applied to a piece of Cu foil with a doctor's blade, dried overnight in a vacuum oven, rolled, and punched to the necessary dimensions for a coin cell. The electrode-equipped CR2032-type battery was installed in an argon-filled glovebox; the electrochemical performance of the prepared samples was examined in Fig. 9-10. The electrolyte used 1 M lithium hexafluorophosphate (LiPF_6) dissolved in co-solvents of ethylene carbonate (EC), dimethyl carbonate (DEC), and ethyl methyl carbonate (EMC) (EC/DEC/EMC = 1:1:1 by volume). The separator used was a Celgard 2325 membrane. The assembled coin cell depicts in Fig. 11.

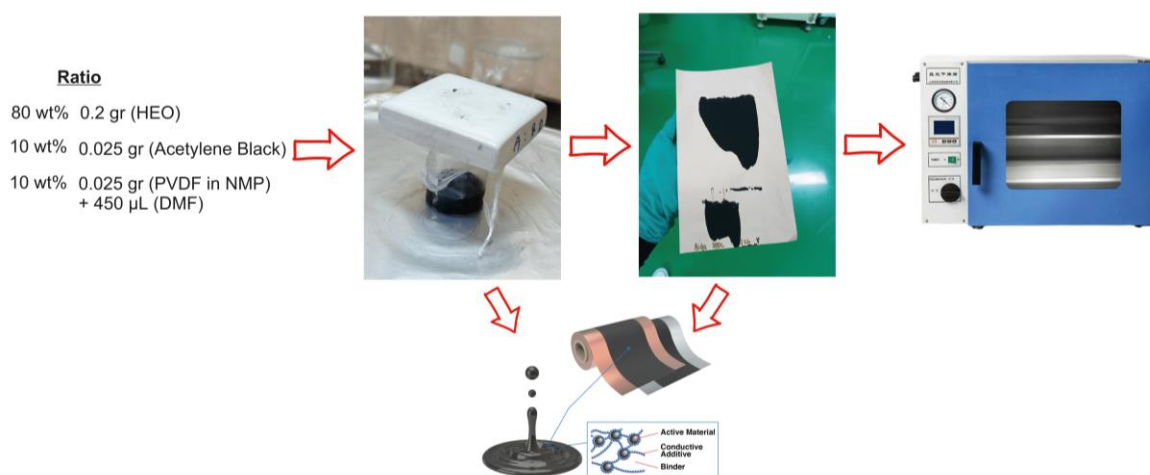


Fig. 9. Electrode preparation using $(\text{FeCoNiMnZn})_3\text{O}_4$.

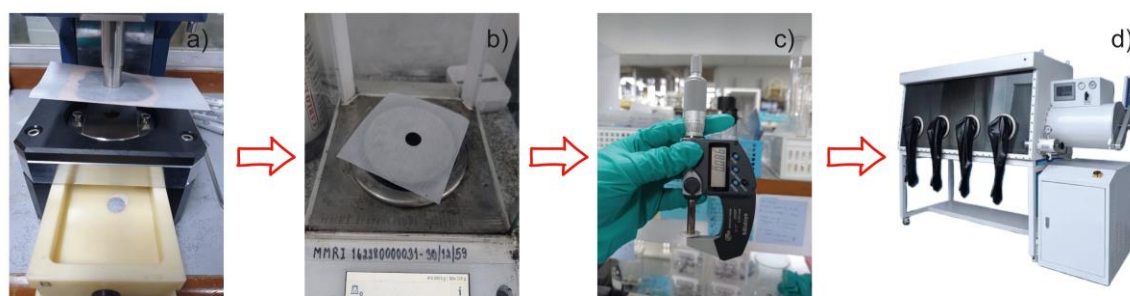


Fig. 10. The steps of cell assembly $(\text{FeCoNiMnZn})_3\text{O}_4$.

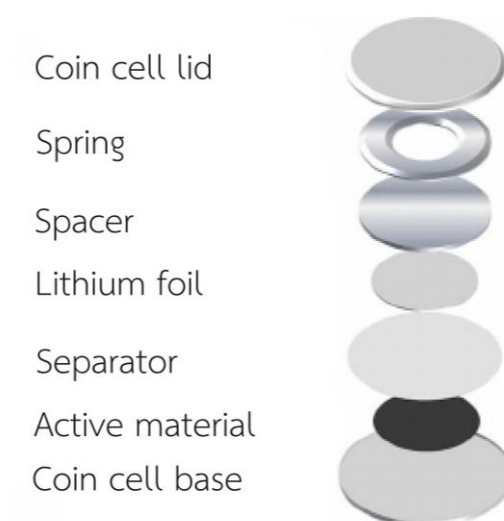


Fig. 11. The sequences of coin cells.

3.3 Characterizations of the Materials and Electrochemistry

The crystalline structure was examined using an X-ray diffractometer (a Rigaku SmartLab 30kV) with a Cu K radiation source set to an accelerating voltage of 40 kV and an applied current of 30 mA. With a scan rate of 5 min^{-1} , the scanned angle spans from 10 to 90. Transmission electron microscopy (TEM, JEOL JSM-IT100 at 20kV) and scanning electron microscopy were used to study the morphology (TEM, Philips brand, Model TECNAI 20). X-ray photoelectron spectroscopy (XPS, Axis Ultra DLD) was used to analyze the surface chemistry. The chemical composition was identified using inductively coupled plasma optical emission spectroscopy (ICP-OES, Thermo Scientific, iCAP 6500). Utilizing the Brunauer-Emmett-Teller equation, the physical adsorption of gas molecules on a solid surface was investigated to measure the specific surface area of materials (BET, Bell Sorp mini II).

With various sweep rates, cyclic voltammetry (CV) was carried out in the potential range of 0.01-3.00 V (vs. Li/Li^+). In the frequency of 0.01- 10^5 Hz, electrochemical impedance spectroscopy (EIS) measurements were made. The battery testing system (BTS, CT-4008, NEWARE, China) was used to assess the charge-discharge characteristics of several cells at room temperature. Current densities were used for charging and discharging between 0.01 and 3.0 V (vs. Li^+/Li).

CHAPTER 4

RESULTS AND DISCUSSION

4.1 Structures and morphologies of $(\text{FeCoNiMnZn})_3\text{O}_4$

4.1.1 X-ray Diffraction (XRD)

An XRD examination of the powder was performed after calcining the produced powder by heating it to various temperatures. The XRD pattern of the samples as-prepared, both before and after calcination, is in Fig. 12. The powder was single-phase with an $\text{Mn}(\text{CO}_3)$ crystal structure. It belonged to the R-3c (167) space group when it was first synthesized, as seen in Fig. 13, and Table 2 is a detailed explanation. However, after calcination at 300°C, one peak showed broad peaks with low ratios of nanocrystalline structure and poor crystallinity. It looked that the position of the broad peaks coincided with a spinel crystal structure. Raising the calcination temperature to 600 °C made the spinel phase's peak sharper with a smaller breadth and a more significant height. In other words, a higher degree of crystallinity made it when the temperature increased. Furthermore, the patterns of three extra broad peaks showed no reflection by $\text{Mn}(\text{CO}_3)$ crystal structure, indicating the decomposition of $\text{Mn}(\text{CO}_3)$ at high temperatures. Eventually, by raising the calcination temperature to 900°C, the XRD pattern showed extremely sharp peaks with higher peaks out of agreement with the single-phase spinel crystal structure. It is the Fd-3m (227) space group in Fig. 14 and detailed information in Table 3. The XRD pattern of the calcined powder at 900°C exhibited sharp peaks with a high degree of crystallinity. Increasing the calcination temperature decreased and rose the peak width and heights, respectively, related to higher degree crystallinity, larger crystallite size, and higher homogeneity.

Divide the synthesis temperature of high entropy oxides into specific points, such as 300, 600, and 900°C, allows for a more detailed investigation of their thermal behavior and phase transformations. Here are why these temperature points are often chosen:

- a) Phase Transitions: The temperature range of 300-900°C covers a range where significant phase transitions or structural changes can occur in HEO [54]. Researchers can identify phase transitions by studying the material's behavior such as crystal structure transformations, lattice parameter changes, or chemical ordering variations at these specific temperature points. Dividing the temperature range helps capture specific thermal events that may impact the material's properties.
- b) Investigation of the thermal stability: Investigating HEO at different temperatures allows for characterizing their stability over various conditions. By examining the material's behavior at lower temperatures, such as 300°C, researchers can assess its stability under typical operating conditions or during processing. Higher temperatures, such as 600 and 900°C, can provide insights into the material's stability at elevated temperatures or in extreme environments.
- c) Characterizing Stability: Investigating HEO at different temperatures allows for describing their stability over various conditions [55]. By examining the material's behavior at lower temperatures, such as 300°C, researchers can assess its stability under typical operating conditions or during processing. Higher temperatures, such as 600 and 900°C, can provide insights into the material's stability at elevated temperatures or in extreme environments.
- d) Thermodynamic Analysis: Dividing the temperature range into specific points facilitates thermodynamic analysis of HEO [56]. Researchers can study the material's Gibbs free energy, enthalpy, entropy, and other thermodynamic properties at these specific temperatures to better understand its stability and phase equilibria. These analyses help establish the material's thermodynamic limits and guide the design of HEO with desired properties.
- e) Property Characterization: The choice of temperature points aligns with practical considerations for property characterization. Certain experimental techniques or measurements may be optimized for specific temperature ranges [57]. Dividing the temperature range into 300, 600, and 900°C intervals allows

researchers to perform in-depth characterizations at these particular points, ensuring comprehensive property analysis and understanding.

- f) Practical Applications: Understanding the behavior of HEO at different temperatures is important for their practical applications. Many potential applications of HEO involve operating at elevated temperatures, such as in high-temperature catalysis, thermal barrier coatings, or extreme environment applications. Investigating the material's properties and stability at temperatures 600 and 900°C helps assess its suitability for these applications.

In summary, dividing the temperature range of HEO into specific points, such as 300, 600, and 900°C, enables a focused examination of their thermal behavior, stability, phase transitions, and thermodynamic properties. Considering the dividing the temperature in calcination, researchers focus on developing electrode materials with good electrical conductivity, optimizing electrode architectures to enhance electron pathways, and exploring conductive additives or coatings. These efforts aim at to improving electron transport, maximizing battery performance, enhancing energy efficiency, and ensure lithium-ion batteries' safe and reliable operation.

Using a low temperature of 300°C for calcination in HEO offers several benefits and drawbacks. Here are the potential advantages and disadvantages:

Benefits of low temperature (300°C) calcination in HEO:

- 1) Energy Efficiency: Calcination at lower temperatures consumes less energy than high-temperature processes, resulting in improved energy efficiency and reduced operational costs [58].
- 2) Reduced Sintering and Particle Growth: Low-temperature calcination minimizes sintering and particle growth, preserving the desired particle size of HEO [59]. This is important when the nanostructured features contribute to functional properties.

Drawbacks of low temperature (300 °C) calcination in HEO:

- 1) Slower Reaction Kinetics: Calcination at lower temperatures generally results in slower reaction kinetics than high-temperature processes [60]. This may require

longer calcination durations to achieve the desired phase transformation or crystal structure evolution in HEO.

- 2) Incomplete Phase Formation: Some HEO may require higher temperatures to achieve complete phase formation or the desired crystal structure [57]. Calcination at 300°C does not fully activate the material or result in the desired phase composition, limiting its functional properties.
- 3) Limited Removal of Volatile Species: Low-temperature calcination may not effectively remove volatile species or impurities from the HEO material [61]. Higher temperatures are often necessary for the complete volatilization or removal of volatile components.
- 4) Reduced Crystal Growth: Lower calcination temperatures may lead to slower crystal growth or incomplete crystallization of HEO. This can affect the material's properties, such as grain size, crystallinity, and long-range ordering.
- 5) Compatibility with Subsequent Processing Steps: If additional thermal treatments or reactions are required after calcination, a low-temperature process might not be compatible. Higher temperatures may be necessary for subsequent process steps, making the overall processing scheme more complex or limiting the material's compatibility with downstream processes.

Depending on the specific composition, desired properties, and application requirements as anode material in lithium-ion batteries, low temperature did not fulfil HEO synthesis.

The peaks in XRD patterns shift, which can provide valuable information about the material's crystal structure and lattice parameters. A growth in the position of XRD peaks towards higher or lower angles indicates a change in the lattice spacing or unit cell dimensions. This can be due to various factors:

- 1) Phase transformation [62]. A change in crystal structure or phase transition can result in peak shifts. For example, a phase change from one crystal structure to another, such as from trigonal (HEO-3) to cubic (HEO-6 & HEO-9), can lead to a shift in the XRD peaks.

- 2) Temperature Effects [63]: Thermal expansion or contraction of the crystal lattice with changing temperature can cause peak shifts in XRD patterns. Higher temperatures can lead to increased lattice spacing.

In addition, the broadening of XRD peaks, without significant shifts in position, indicates a decrease in crystallite size [64, 65]. This can be due to factors such as:

- 1) The finite size effect can lead to peak broadening in the XRD pattern when the material consists of nanocrystalline domains or nanoparticles. Smaller crystallite sizes result in broader diffraction peaks.
- 2) Disorder or Amorphousness: If the material is partially amorphous or contains a disordered phase, the XRD peaks may be broadened due to the lack of long-range order.

In summary, shifts in XRD peaks provide insights into changes in lattice parameters, phase transformations, or temperature effects. Peak broadening indicates variations in crystallite size, lattice defects, or disorder within the material.

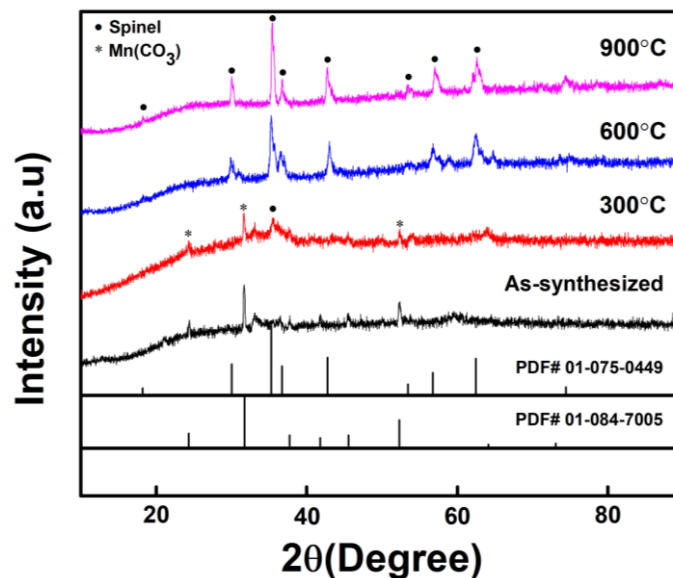


Fig. 12. XRD patterns of HEO-NP at different temperatures and as-synthesized.

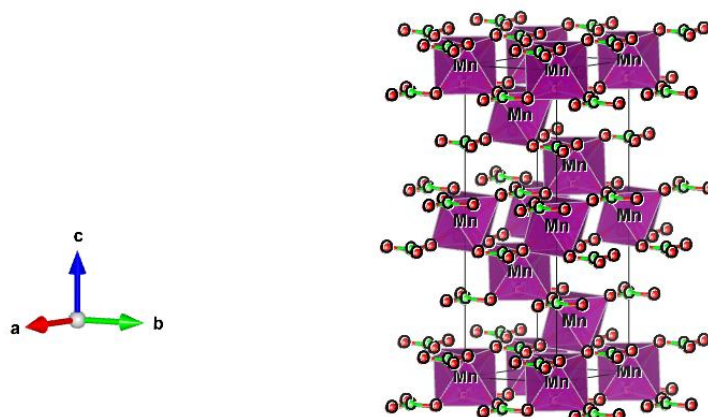


Fig. 13. Unit cell of rhodochrosite crystal structure.

Table 2. The detail information about rhodochrosite crystal structure.

Title				Mn (CO ₃)			
Lattice type				R			
Space group name				R -3 c			
Space group number				167			
Lattice parameters	a	b	c	Alpha	beta	gamma	
	4.77300	4.77300	15.64200	90.0000	90.0000	120.0000	
Unit-cell volume				308.606980 Å ³			
Structure parameters	x	y	z	Occ.	U	Site	Sym.
Mn	0.00000	0.00000	0.00000	1.000	0.000	6b	-3.
C	0.00000	0.00000	0.25000	1.000	0.000	6a	32
O	0.26950	0.00000	0.25000	1.000	0.000	18e	.2

In summary, the crystal structure of rhodochrosite Mn (CO₃) consists of manganese (Mn) ions and carbonate (CO₃) ions arranged in a specific pattern. In rhodochrosite, the Mn²⁺ ions occupy octahedral sites within the crystal structure. Each Mn²⁺ ion is coordinated with six carbonate ions (CO₃), forming an octahedral coordination geometry. The carbonate ions surround the central Mn²⁺ ion, with three carbonate ions in the equatorial plane and three carbonate ions above and below the plane.

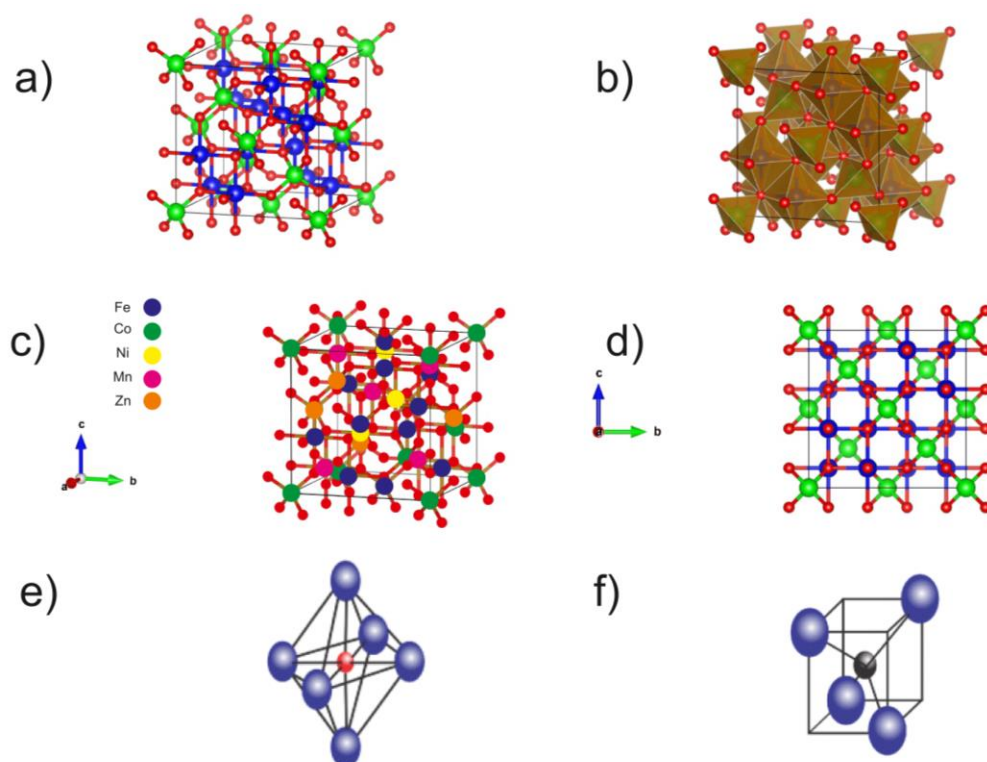


Fig. 14. a) Unit cell of the spinel structure, b) in a polyhedral form where red (oxygen); green (tetrahedral site); blue (octahedral site), c) a schematic illustration of the structure of HEO, d) view along an axis, the figure of octahedral site e) and tetrahedral site f).

Table 3. The detail information about magnetite crystal structure.

Title			Fe ₃ O ₄ (magnetite)				
Lattice type			F				
Space group name			F d -3 m				
Space group number			227				
Lattice parameters	a	b	c	Alpha	beta	gamma	
	8.32000	8.32000	8.32000	90.0000	90.0000	90.0000	
Unit-cell volume			575.930305 Å ³				
Structure parameters	x	y	z	Occ.	U	Site	Sym.

Fe1	0.00000	0.00000	0.00000	1.000	0.000	8a	-43m
Fe2	0.62500	0.62500	0.62500	1.000	0.000	16d	-.3m
O	0.37500	0.37500	0.37500	1.000	0.000	32e	.3m

In conclusion, the distribution of Fe^{3+} and Fe^{2+} ions within the octahedral and tetrahedral sites and the magnetite gives many interesting physical and chemical properties, such as its ability to undergo electron transfer reactions, redox properties, and catalytic activity.

Each basic oxide was also synthesized, and Fig. 15 shows their XRD patterns. A summary of the detailed information about crystal structure is in Table 4. Firstly, iron oxides have hematite for the unit cell in Fig. 16; details can be seen in Table 5. Secondly, Fig. 17 shows the cobalt dicobalt (III) oxide crystal structure; Table 6 is specific. Next, a unit cell of NiO is in Fig. 18 and Table 7. Bixbyite crystal structure of manganese oxides is described in Fig. 19 and Table 8. Also, ZnO only has a hexagonal crystal structure in Fig. 20, and the explanation is in Table 9.

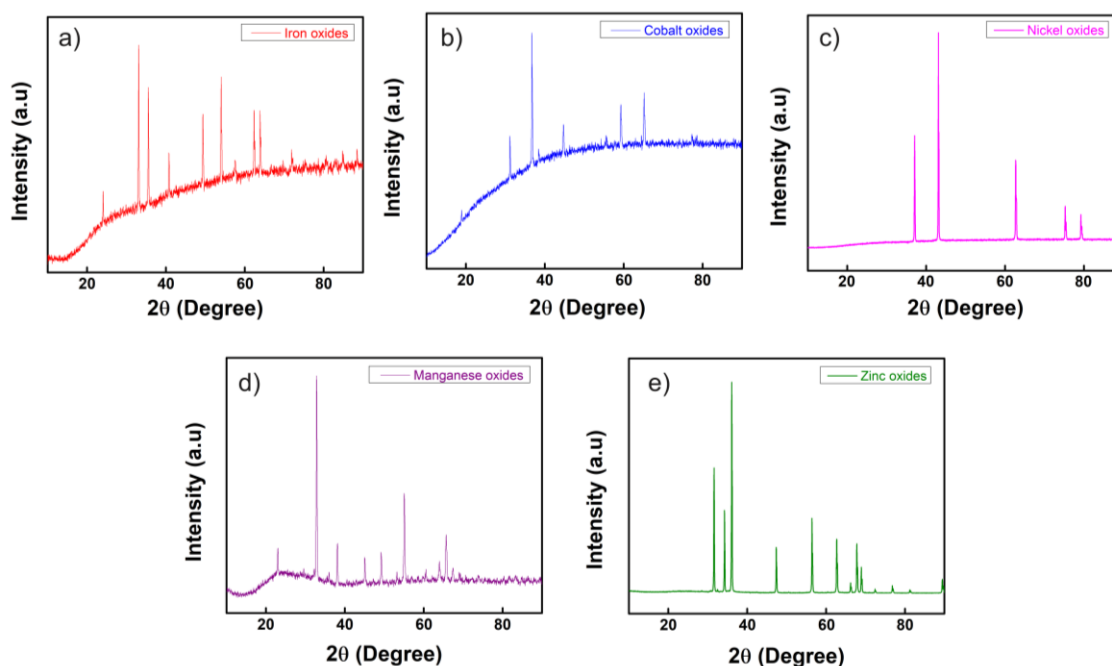


Fig. 15. XRD patterns of a) Iron oxide in comparison with reference (PDF#00-033-0664), b) Cobalt oxide in comparison with reference (PDF#01-080-1533), c) Nickel in

comparison with reference (PDF#01-078-4374), d) Manganese in comparison with reference (PDF#01-089-2809), and e) Zinc in comparison with reference (PDF#01-080-0075).

Table 4. Summary of each metal oxide of Fe, Co, Ni, Mn, Zn, and HEO.

Oxides	Chemical Formula	Space Group	Crystal Structure
Iron	Fe ₂ O ₃ (Hematite, syn)	R-3c (167)	Trigonal
Cobalt	Co ₃ O ₄ (Cobalt dicobalt (III) oxide)	Fd-3m (227)	Cubic
Nickel	NiO (Nickel oxide)	R-3m (166)	Trigonal
Manganese	Mn ₂ O ₃ (Bixbyte, syn)	Ia-3 (206)	Cubic
Zinc	ZnO (Zinc oxide)	P63mc (186)	Hexagonal
HEO-3	Mn (CO ₃) (rhodochrosite)	R-3c (167)	Trigonal
	Fe ₃ O ₄ (Magnetite)	Fd-3m (227)	Cubic
HEO-6 & HEO-9	Fe ₃ O ₄ (Magnetite)	Fd-3m (227)	Cubic

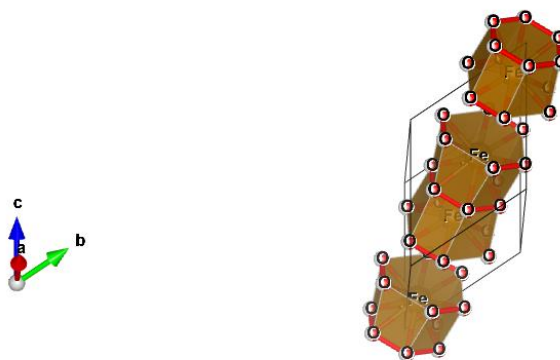


Fig. 16. Unit cell of hematite crystal structure.

Table 5. The detail information about hematite crystal structure.

Title	Fe ₂ O ₃ (hematite)
Lattice type	R

Space group name				R -3 c (The R-3c space group refers to a rhombohedral crystal system with a threefold rotational symmetry axis)			
Space group number				167			
Lattice parameters	a	b	c	Alpha	beta	gamma	
	5.43000	5.43000	5.43000	55.2800	55.2800	55.2800	
Unit-cell volume				100.791618 Å ³			
Structure parameters	x	y	z	Occ.	U	Site	Sym.
Fe	0.10500	0.10500	0.10500	1.000	0.000	4c	3.
O	0.29200	- 0.29200	0.00000	1.000	0.500	12f	1

In summary, the crystal structure of Fe₂O₃ (hematite) in the R-3c space group consists of iron (Fe) ions in the +3 oxidation state surrounded by oxygen (O) ions in an octahedral coordination arrangement.

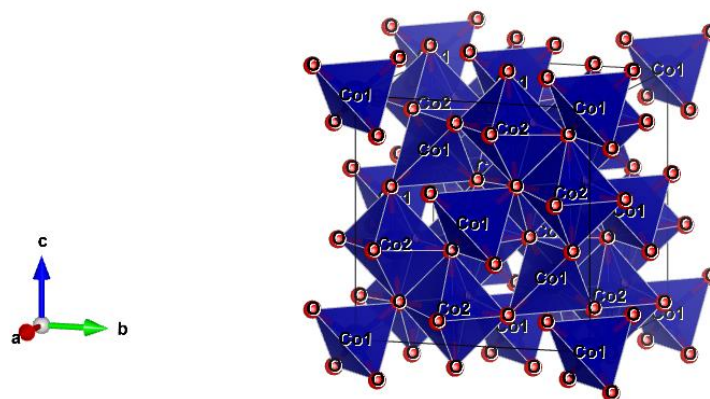


Fig. 17. Unit cell of Cobalt dicobalt (III) oxide crystal structure.

Table 6. The detail information about Cobalt dicobalt (III) oxide crystal structure.

Title	Co ₃ O ₄ (Cobalt dicobalt (III) oxide)
Lattice type	F

Space group name			F d -3 m (The "F" indicates that the unit cell is face-centered, the "d" means that the lattice is diamond-shaped, and the "-3m" indicates the specific symmetry elements present in the crystal structure)				
Space group number			227				
Lattice parameters	a	b	c	Alpha	beta	gamma	
	8.06500	8.06500	8.06500	90.0000	90.0000	90.0000	
Unit-cell volume			524.581593 Å ³				
Structure parameters	x	y	z	Occ.	U	Site	Sym.
Co2	0.62500	0.62500	0.62500	1.000	0.000	16d	.-3m
O	0.38800	0.38800	0.38800	1.000	0.000	32e	.3m
Co1	0.00000	0.00000	0.00000	1.000	0.000	8a	-43m

In summary, the crystal structure of Co_3O_4 in the $Fd\text{-}3m$ space group consists of cobalt (Co) ions in both the +2 and +3 oxidation states surrounded by oxygen (O) ions in tetrahedral coordination arrangements.

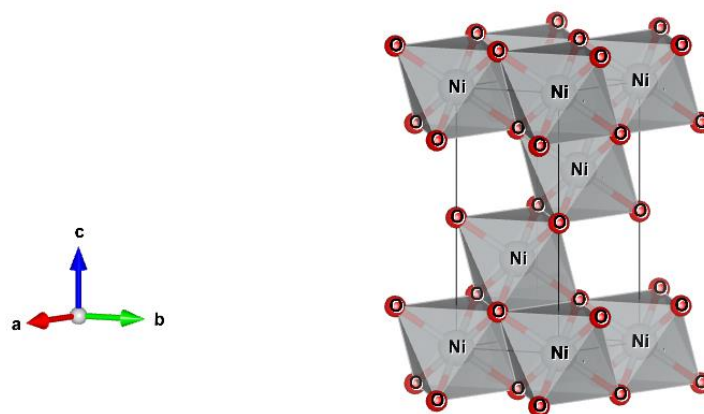


Fig. 18. Unit cell of nickel oxide crystal structure.

Table 7. The detail information about nickel oxides crystal structure.

Title		NiO					
Lattice type		R					
Space group name		R -3 m (The "R" denotes a rhombohedral unit cell, and the "-3m" signifies specific symmetry elements present in the crystal structure)					
Space group number		166					
Lattice parameters	a	b	c	Alpha	beta	gamma	
	2.95170	2.95170	7.21700	90.0000	90.0000	120.0000	
Unit-cell volume		54.454247 Å ³					
Structure parameters	x	y	z	Occ.	U	Site	Sym.
Ni	0.00000	0.00000	0.00000	1.000	0.000	3a	-3m
O	0.00000	0.00000	0.50000	1.000	0.000	3b	-3m

In summary, the crystal structure of NiO in the R-3m space group consists of nickel (Ni) ions in the +2 oxidation state surrounded by oxygen (O) ions in an octahedral coordination arrangement.

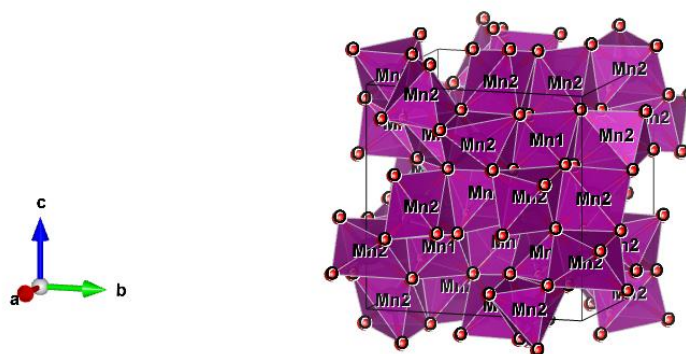


Fig. 19. Unit cell of bixbyite crystal structure.

Table 8. The detail information about bixbyite crystal structure.

Title		Mn ₂ O ₃ (Bixbyite)					
Lattice type		I					
Space group name		I a -3 (The "I" denotes a body-centered unit cell, the "a" signifies a cubic lattice type, and the "-3" represents specific symmetry elements present in the crystal structure)					
Space group number		206					
Lattice parameters	a	b	c	Alpha	beta	gamma	
	9.42000	9.42000	9.42000	90.0000	90.0000	90.0000	
Unit-cell volume		835.896908 Å ³					
Structure parameters	x	y	z	Occ.	U	Site	Sym.
Mn1	0.25000	0.25000	0.25000	1.000	0.250	8b	.-3.
Mn2	-0.03470	0.00000	0.25000	1.000	0.210	24d	2..
O	0.37800	0.16700	0.37900	1.000	0.500	48e	1

In summary, the crystal structure of Mn₂O₃ in the Ia-3 space group consists of manganese (Mn) ions in the +3 oxidation state surrounded by oxygen (O) ions in octahedral coordination.

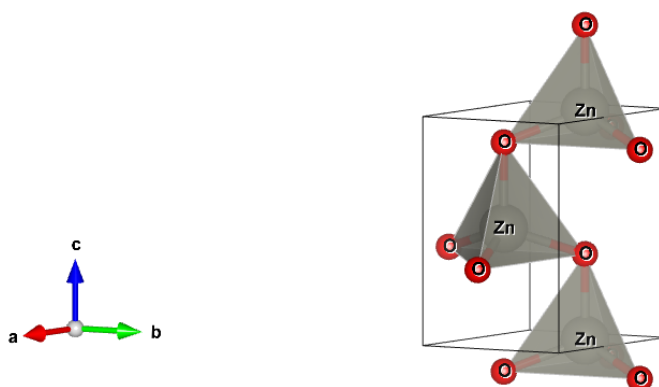


Fig. 20. Unit cell of zinc oxide crystal structure.

Table 9. The detail information about Zinc oxide crystal structure.

Title		O Zn					
Lattice type		P					
Space group name		P 63 m c (The "P" denotes a primitive unit cell, the "6" represents the sixfold rotational symmetry, and the "mc" signifies a mirror plane perpendicular to the c-axis)					
Space group number		186					
Lattice parameters	a	b	c	Alpha	beta	gamma	
	3.22000	3.22000	5.20000	90.0000	90.0000	120.0000	
Unit-cell volume		46.692348 Å ³					
Structure parameters	x	y	z	Occ.	U	Site	Sym.
Zn	0.33333	0.66667	0.00000	1.000	0.000	2b	3m.
O	0.33333	0.66667	0.37500	1.000	0.000	12b	3m.

In summary, the crystal structure of ZnO in the P63mc space group consists of zinc (Zn) ions in the +2 oxidation state surrounded by oxygen (O) ions in tetrahedral coordination.

4.1.2 X-ray photoelectron spectroscopy (XPS)

Formation Mechanism

As previously noted, CTAB was the surfactant during the synthesis since it effectively regulates the nanoparticle size and form. According to Fig. 21 and Reactions (3) – (5), CTAB hydrolyzes urea in the solution before the hydrothermal synthesis and generates CTA⁺ and Br⁻. The formation of metal hydroxy carbonates and carbonates in hydrothermal processes follows Reactions (6) and (7). Following the heat treatment, as demonstrated in Reaction (8).

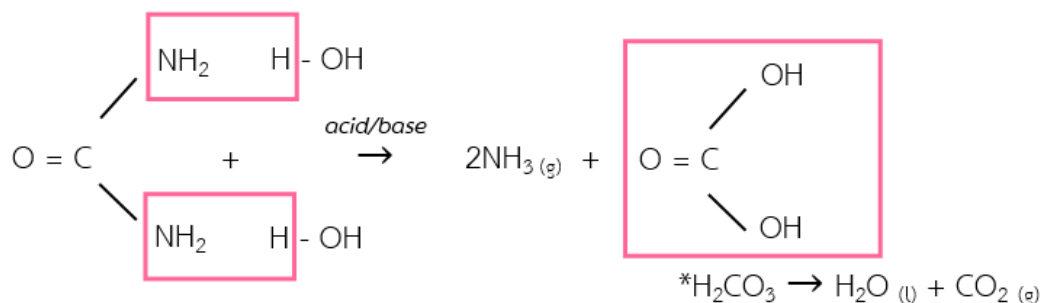
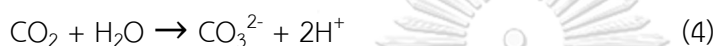
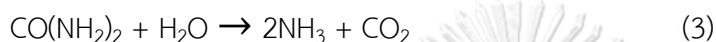


Fig. 21. The reaction of urea hydrolysis.



To determine the chemical compositions and oxidation states of (FeCoNiMnZn)₃O₄ particles at 600°C in Fig. 22 and at 900°C in Fig 23, XPS analysis was carried out on the powder samples. The complete spectroscopy of HEO-9 detected Fe, Co, Ni, Mn, Zn, and O, shown in Fig. 24. The outcomes also show that the powders were successfully produced, and the samples were uncontaminated. The HEO nanoparticles' whole cation population is in the +2 state, which is appropriate with the reported in earlier research [66-68]. The Fe 2p spectra of samples with two spin-orbits are shown in Fig. 23a. Fe²⁺ is linked to the peaks at 709.8 and 722.8 eV, while Fe³⁺ is connected to the peaks at 713 and 724.3 eV. In Fig. 23b, Co 2p is depicted. Peaks at 782.3 eV (Co 2p_{3/2}) and 797.4 eV (Co 2p_{1/2}) are referred to as Co²⁺, whereas peaks at 779.2 eV (Co 2p_{3/2}) and 795.7 eV (Co 2p_{1/2}) are associated with Co³⁺. Then, in Fig. 23c, Ni 2p is depicted, with Ni²⁺ peaks at 854.9 eV (Ni 2p_{3/2}) and 872.5 eV (Ni 2p_{1/2}) and Ni³⁺ peaks at 856.6 eV (Ni 2p_{3/2}) and 874.1 eV (Ni 2p_{1/2}), respectively. Additionally, Mn 2p is shown in Fig. 23d; the peaks for Mn³⁺ are at 640.7 eV (Mn 2p_{3/2}) and 652.3 eV (Mn 2p_{1/2}), while those for Mn⁴⁺ are at 644.3 eV (Mn 2p_{3/2}) and 653.6 eV, respectively. The binding energies of Zn²⁺ in Fig. 23e are 1021.3 and 1044.5 eV, corresponding to Zn 2p_{3/2}

and Zn $2p_{1/2}$, respectively. Three regions can suit the O 1s peak in Fig. 23f. The chemisorbed oxygen (O_C) peak at 533.3 eV can be attributed to the chemically and physically adsorbed water on the material surface. The rise of oxygen in the lattice (O_L) at 528.9 eV represents M-O in metal oxide; the peak of oxygen vacancy (O_V) at 531.8 eV corresponds to a high number of defect sites with low oxygen coordination in the material. Electron transport may be aided by O_V , which would support electrochemical capabilities.

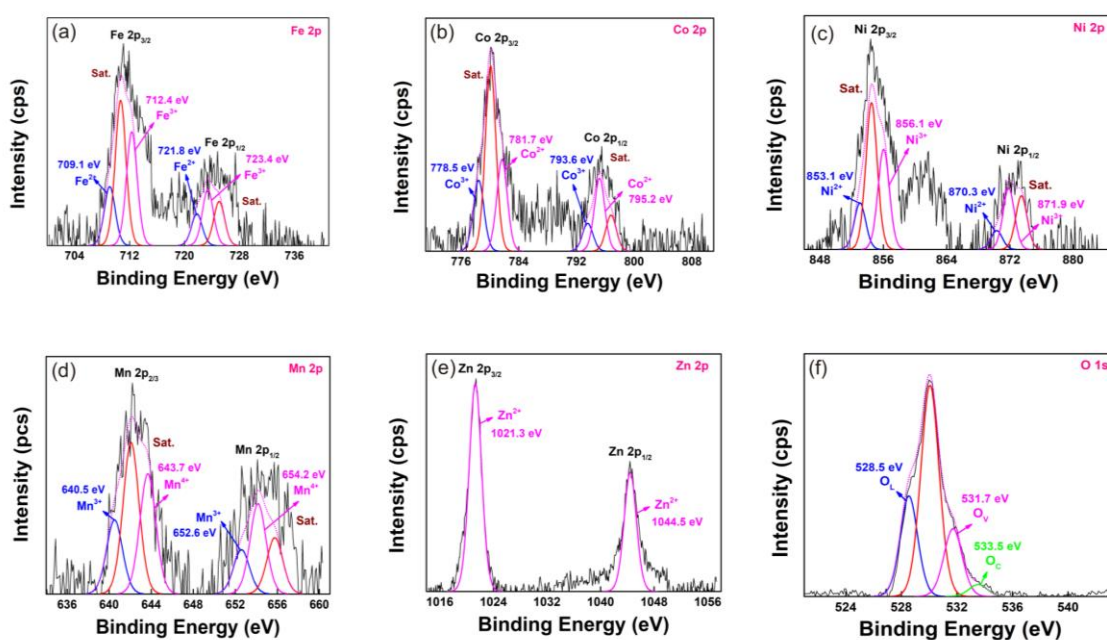


Fig. 22. XPS images of HEO-6 a) Fe 2p, b) Co 2p, c) Ni 2p, d) Mn 2p, e) Zn 2p, and f) O 1s spectra.

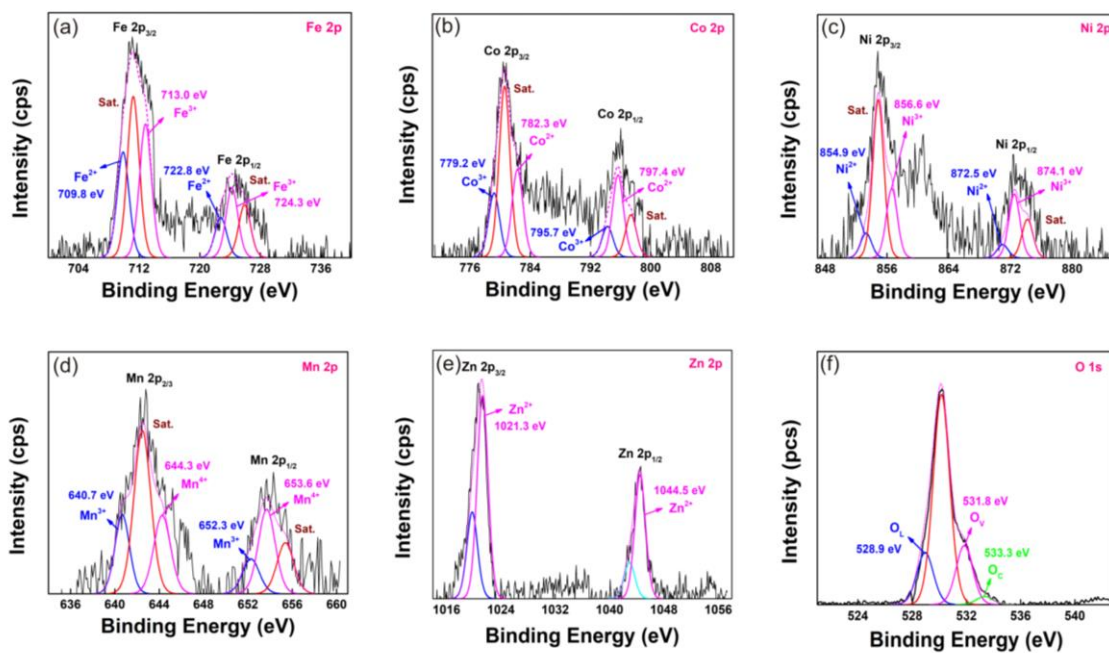


Fig. 23. XPS images of HEO-9 a) Fe 2p, b) Co 2p, c) Ni 2p, d) Mn 2p, e) Zn 2p, and f) O 1s spectra.

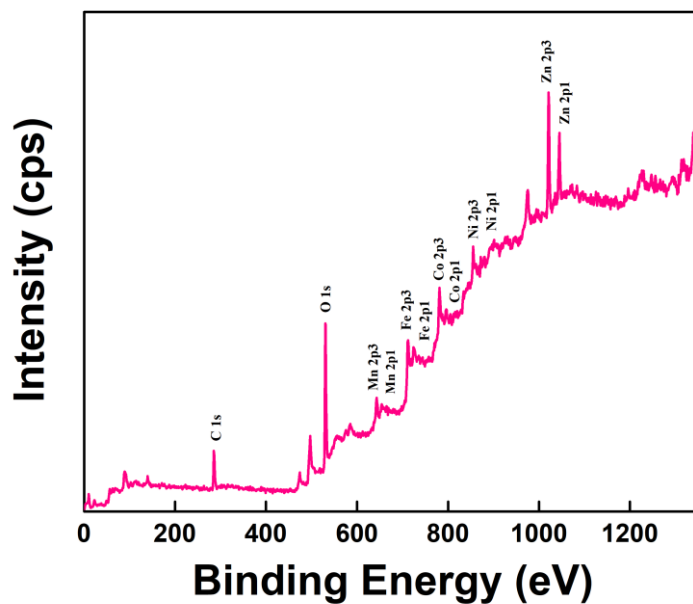


Fig. 24. XPS complete spectroscopy of HEO-9.

4.1.3 Scanning Electron Microscope (SEM)

The high-entropy nanoparticles morphology was determined utilizing SEM analysis, as shown in Fig. 25, which shows that the sample was made up of semi-spherical particles. Nanoparticles and sub-micro size particles can also be detected in the particle size histogram. As previously mentioned, SEM patterns and the size of basic oxide are also investigated in Fig. 26. They have different shapes. The particle size of HEO-6 and HEO-9 are 110–200 nm and 140–260 nm. In other words, bigger particle size was associated with increased calcination. Meanwhile, HEO-3 cannot be measured because it is too small and impure. In the hydrothermal method for synthesizing high-entropy oxides, low temperatures of HEO-3 are often employed to promote the formation of small particle sizes. This phenomenon can be attributed to several factors [69, 70]:

- 1) Nucleation and Growth: at lower temperatures, the rate of nucleation, which is the initial formation of particles, is favored. With a higher nucleation rate, smaller particles are formed due to the limited availability of precursor materials for growth. As a result, the particles remain small in size.
- 2) Precursor Solubility: lower temperatures can decrease the solubility of precursors in the hydrothermal solution. When the solubility is reduced, reactants' availability decreases, limiting particle growth. Consequently, smaller particles are favored.
- 3) Reaction Rate: reactions occurring at lower temperatures tend to proceed slower. Slower reaction rates can impede particle growth, leading to smaller particles forming over extended periods.
- 4) Agglomeration Prevention: In hydrothermal synthesis, there is a risk of particles aggregating or merging to form larger particles. The use of low temperatures can help mitigate this issue by reducing the mobility and diffusion of particles, thus hindering their aggregation and resulting in smaller particle sizes.

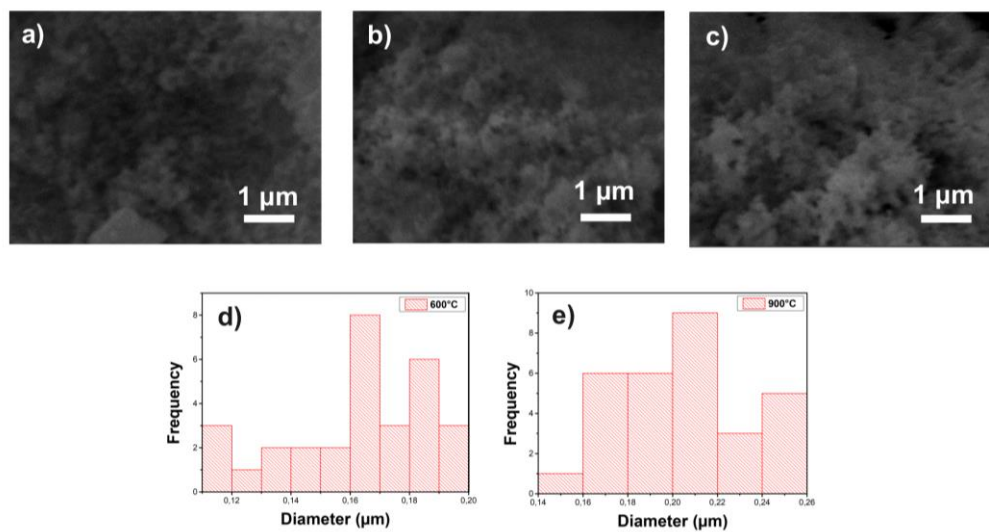


Fig. 25. SEM images and histograms of the particle size distribution of a) HEO-3, b) HEO-6, and c) HEO-9.

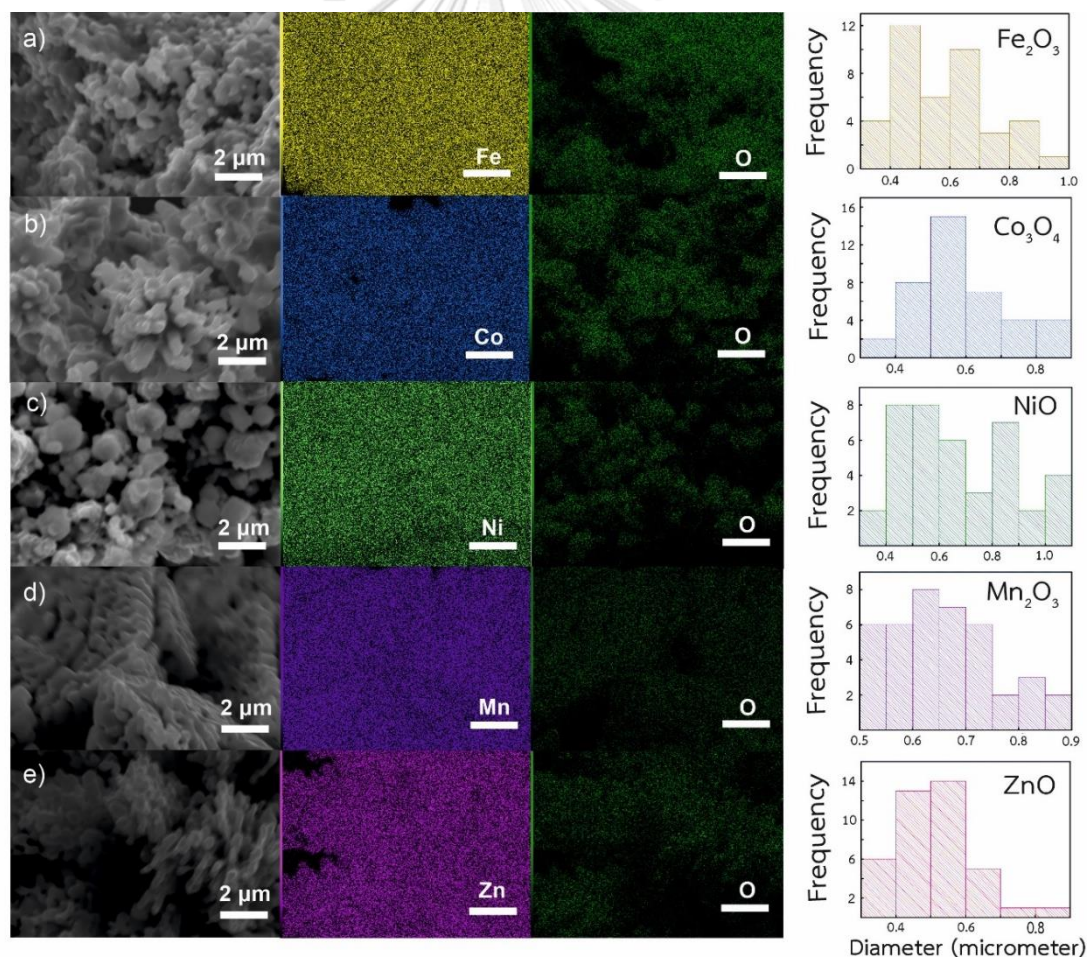


Fig. 26. SEM image and histogram of particle size of a) Fe, b) Co, c) Ni, d) Mn, and e) Zn oxides.

The particle size of HEO is generally smaller than that of individual elemental oxides in Fig. 27 due to some reasons [71, 72]:

1. Increased atomic disorder: High entropy oxides consist of multiple cations with varying atomic sizes. This high degree of atomic disorder disrupts the regular lattice structure of the oxide. The lack of long-range order in HEO prevents the formation of large crystalline domains, resulting in smaller particle sizes.
2. HEO have a higher surface energy than individual elemental oxides due to their complex structure. This increased surface energy promotes the formation of smaller particles to minimize the material's overall surface area and energy.
3. Thermodynamic stability: High entropy oxides often exhibit improved thermodynamic stability compared to binary oxides. The enhanced stability arises from forming a solid solution with a more random distribution of cations, reducing the driving force for phase separation and grain growth. As a result, the particles tend to remain smaller and more stable over a wide range of conditions.

Overall, the smaller particle size of HEO can offer several advantages over individual elemental oxides, including improved reactivity, catalytic activity, and surface area.

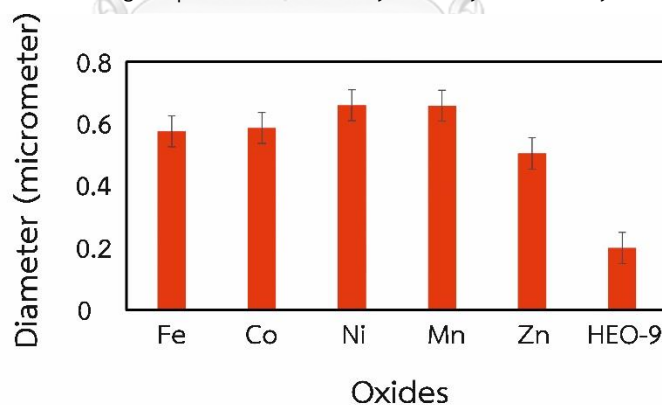


Fig. 27. The distribution of diameter of each elemental and high-entropy oxide.

4.1.4 Energy dispersive X-ray spectroscopy (EDS)

EDS elemental mapping pictures for high-entropy oxides demonstrated distinct dispersion, and Fe, Co, Ni, Mn, Zn, and O were distributed uniformly. EDS mapping analysis was used to ascertain the components' homogeneity and random distribution

at the nanoscale. The related EDS elemental maps for the HEO-3, HEO-6, and HEO-9 are shown in Fig. 28, 29, and 30, respectively. The outcomes showed no element segregation in any individual HEO nanoparticle and a consistent distribution of all the elements among all the particles. These outcomes support the XRD findings and demonstrate how HEO powder was created.

The elemental distribution measured using Energy Dispersive X-ray Spectroscopy (EDS) shows a similar atomic ratio, as seen in Table 10-12. Also, the elemental of Fe, Co, Ni, Mn, and Zn has detailed in Table 13. They are quite similar corresponding to the oxygen of each metal. It typically indicates that the analyzed sample has a consistent elemental composition throughout the surveyed area. This means that the relative amounts of different elements present in the sample are relatively constant or proportionate to each other. Having a similar atomic ratio in EDS analysis can suggest several things:

- 1) Homogeneous Composition: a consistent atomic ratio implies that the sample has a uniform elemental distribution, meaning the composition of the material is consistent across the analyzed area. This is often desirable when analyzing homogeneous materials or studying specific regions of interest.
- 2) Chemical Composition Confirmation: a similar atomic ratio confirms that the elements are present in the expected proportions if the sample's composition is known or expected. This can provide validation that the sample matches the anticipated composition.
- 3) Stoichiometry: in the case of compounds, a similar atomic ratio in EDS analysis indicates that the elements are present in the expected stoichiometric ratio. This suggests that the sample contains the details in the appropriate proportions for forming the compound.

Suppose the elemental atoms in high-entropy oxides are present in similar or exact amounts. In that case, it implies that the oxide composition is highly balanced and exhibits a high degree of entropy. This concept is central to high-entropy materials, where multiple elements are combined in approximately equimolar ratios. Traditional oxide materials typically contain one or a few dominant details with minor dopants or

impurities. However, high-entropy oxides depart from this conventional approach by incorporating several aspects in nearly equal proportions. The rationale behind this is to introduce compositional disorder and enhance the configurational entropy of the material. By having similar amounts of different elemental atoms, high-entropy oxides aim to maximize the number of potential configurations and mixing arrangements at the atomic level. This increased configurational entropy can lead to unique structural, mechanical, thermal, and chemical properties compared to conventional materials. High-entropy oxides have gained attention for their potential in catalysis, energy storage, electronic applications, and other fields due to their promising properties from the diverse combination of elements.

Table 10. Elemental percentages of $(\text{FeCoNiMnZn})_3\text{O}_4$ at 300°C.

Formula	Mass (%)	Atom (%)	Sigma	Net	K ratio	Line
C	59.90	71.69	0.06	61860	0.0155139	K
O	28.27	25.40	0.19	14012	0.0119344	K
Mn	2.60	0.68	0.06	5702	0.0053770	K
Fe	2.05	0.53	0.05	3925	0.0042817	K
Co	2.98	0.73	0.06	4744	0.0061012	K
Ni	2.16	0.53	0.07	2930	0.0044940	K
Zn	2.03	0.45	0.08	1884	0.0039483	K
Total	100.00	100.00				

Table 11. Elemental percentages of $(\text{FeCoNiMnZn})_3\text{O}_4$ at 600°C.

Formula	Mass (%)	Atom (%)	Sigma	Net	K ratio	Line
C	73.52	81.94	0.06	93348	0.0234109	K
O	19.74	16.52	0.19	7781	0.0066276	K
Mn	1.09	0.27	0.04	2504	0.0023616	K
Fe	1.28	0.31	0.04	2556	0.0027882	K
Co	1.69	0.38	0.05	2787	0.0035834	K
Ni	1.54	0.35	0.05	2186	0.0033539	K

Zn	1.13	0.23	0.07	1094	0.0022923	K
Total	100.00	100.00				

Table 12. Elemental percentages of $(\text{FeCoNiMnZn})_3\text{O}_4$ at 900°C.

Formula	Mass (%)	Atom (%)	Sigma	Net	K ratio	Line
C	5.12	16.15	0.01	25236	0.0035583	K
O	12.98	30.76	0.03	184243	0.0851389	K
Mn	14.32	9.88	0.07	101749	0.1305672	K
Fe	18.46	12.53	0.08	108384	0.1684948	K
Co	17.12	11.01	0.09	78497	0.1535344	K
Ni	16.74	10.81	0.10	61041	0.1519053	K
Zn	15.26	8.85	0.14	33163	0.1290657	K
Total	100.00	100.00				

Table 13. Elemental percentages of each basic oxide.

Iron oxides		Cobalt oxides		Nickel oxides		Manganese oxides		Zinc oxides	
Fe	O	Co	O	Ni	O	Mn	O	Zn	O
(%)	(%)	(%)	(%)	(%)	(%)	(%)	(%)	(%)	(%)
44.80	55.20	53.53	46.47	66.79	33.21	40.18	59.82	57.24	42.76

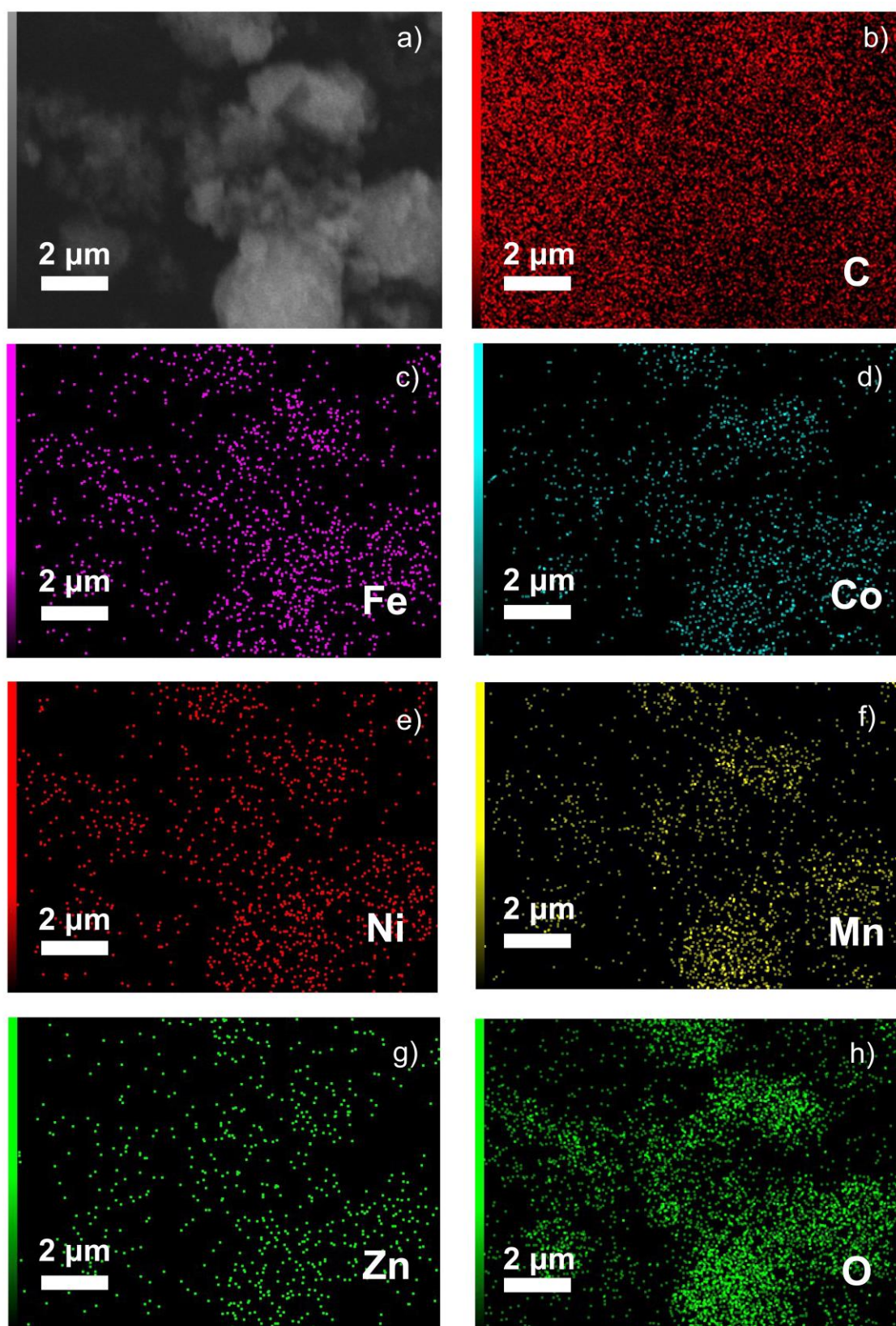


Fig. 28. EDS elemental mapping images of $(\text{FeCoNiMnZn})_3\text{O}_4$ at 300°C .

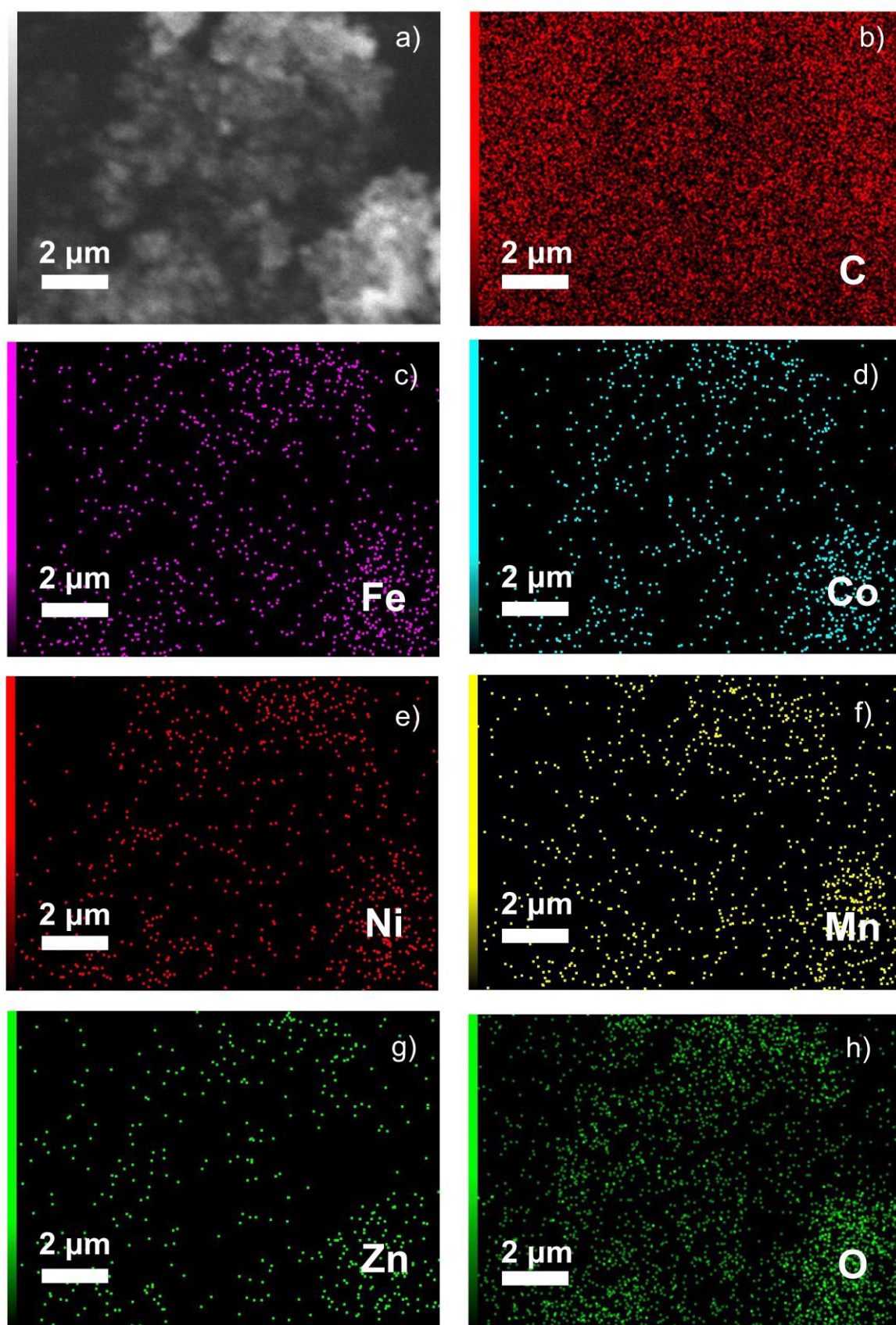


Fig. 29. EDS elemental mapping images of $(\text{FeCoNiMnZn})_3\text{O}_4$ at 600°C .

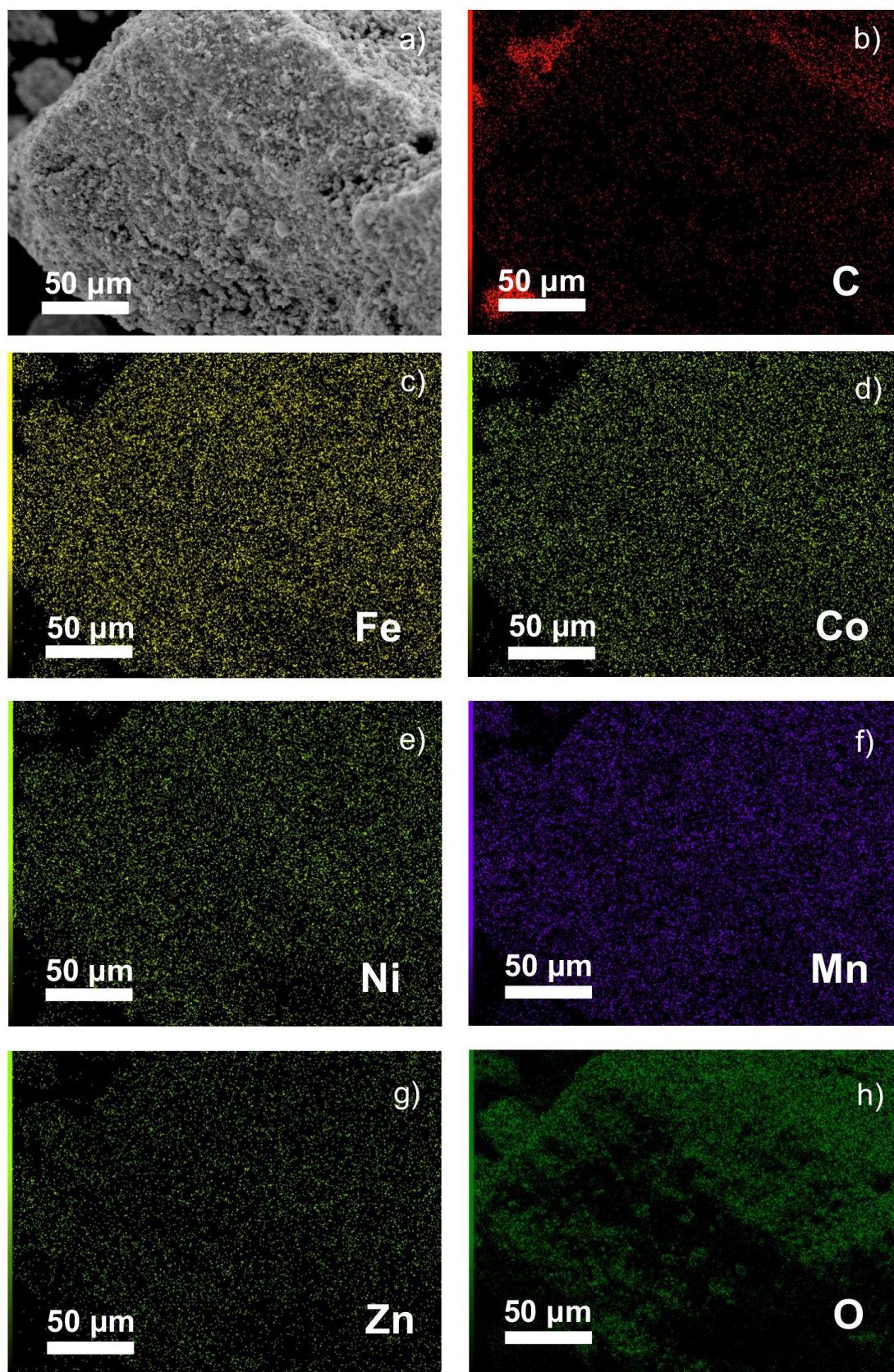


Fig. 30. EDS elemental mapping images of $(\text{FeCoNiMnZn})_3\text{O}_4$ at 900°C .

4.1.5 Inductively coupled plasma optical emission spectroscopy (ICP-OES)

As seen, the components are evenly dispersed throughout the nanoparticles. To determine the chemical composition of the collected samples, ICP-OES tests were made. ICP analysis is often considered more reliable than EDX analysis for elemental distribution for several reasons:

- a) Sensitivity and Detection Limit: ICP analysis typically offers higher sensitivity and lower detection limits than EDX analysis. ICP can detect trace elements at much lower concentrations, allowing for more accurate and precise measurements of element distribution, even in samples with low elemental concentrations.
- b) Wide Elemental Coverage: ICP analysis covers more elements than EDX. While both techniques can detect various features, ICP analysis is particularly well-suited for analyzing elements across the periodic table, including metals and non-metals. This comprehensive coverage is valuable for elemental distribution studies where a diverse set of components may be of interest.
- c) Quantitative Analysis: ICP analysis is generally more accurate in providing quantitative results for elemental distribution [73]. It allows for precisely determining elemental concentrations in a sample, enabling reliable measurements of element distribution across different regions. EDX analysis, on the other hand, may have limitations in the quantitative analysis due to factors such as matrix effects, spectral interferences, and constraints in calibration standards.
- d) Simultaneous Multielement Analysis: ICP analysis can perform simultaneous multielement analysis, measuring the concentration of multiple elements in a sample. This capability allows for efficient and time-saving analysis, particularly in complex samples or when many elements must be analyzed. In contrast, EDX analysis typically requires sequential scanning and analysis, making it more time-consuming.
- e) Accuracy and Precision: ICP analysis generally provides higher accuracy and precision due to its superior detection limits, calibration methods, and lower

interference effects. It can achieve better reproducibility in measurements, reducing errors and uncertainties in elemental distribution analysis.

- f) Sample Compatibility: ICP analysis is compatible with various sample types, including liquids, solutions, and solid samples (coupled with sample digestion techniques) [74]. This versatility allows for analyzing various sample matrices, making them suitable for applications and sample types. EDX analysis, on the other hand, is primarily used for solid samples, limiting its application range.

While ICP analysis offers several advantages over EDX for elemental distribution studies, it is worth noting that both techniques have their respective strengths and limitations. The choice of the most appropriate technique depends on the specific requirements of the analysis, sample type, elemental coverage, and desired sensitivity and accuracy.

All three examples have quite comparable features, as seen in Table 14. HEO-3, HEO-6, and HEO-9 each have computed entropy configuration values of 1.593R, 1.591R, and 1.584R, respectively.

Table 14. ICP-OES concentration and corresponding calculated entropy configuration values of the obtained samples.

ID	Fe (%)	Co (%)	Ni (%)	Mn (%)	Zn (%)	ΔS
HEO-3	20.62	18.14	14.43	25.36	21.44	1.5927R
HEO-6	19.80	17.62	14.26	24.75	23.56	1.5905R
HEO-9	16.82	17.89	14.67	26.65	23.97	1.5841R

e.g. $\Delta S_{\text{HEO-9}} = -R (0.16 \ln 0.16 + 0.18 \ln 0.18 + 0.15 \ln 0.15 + 0.27 \ln 0.27 + 0.24 \ln 0.24) = -1.58R$

The existence of Zn in high entropy oxides refers to the presence of zinc as one of the constituent elements in the composition of these materials. In high entropy oxides, the incorporation of Zn serves several purposes:

- 1) Composition and Property Tuning: Including Zn allows for the adjustment of the material's composition, enabling the fine-tuning of its properties. Since high entropy oxides consist of multiple elements, including Zn provides an additional element to control the material's chemical and physical characteristics [75].
- 2) Synergistic Effects: The presence of Zn in high entropy oxides can contribute to synergistic effects among the constituent elements. Combining different elements, including Zn, in equimolar ratios can lead to unique and enhanced properties that are not typically observed in single-component or binary oxides.
- 3) Structural Stability: Zn can enhance the structural stability of high entropy oxides [76]. Its presence can contribute to the formation of solid solutions or stabilize specific crystal structures, thus improving the overall stability of the material.

Incorporating Zn in high entropy oxides provides additional flexibility in tailoring these materials' composition, properties, and performance. By incorporating multiple elements, including Zn, in equimolar ratios, high entropy oxides offer unique opportunities to explore novel materials with enhanced or multifunctional properties.

If Zn is removed from the compound, there will be some effects. As *Sarkar et al.* [22] were done which first demonstrated HEO as an anode for lithium-ion batteries, they compared 5 cations HEO, $(\text{Co}_{0.2}\text{Cu}_{0.2}\text{Mg}_{0.2}\text{Ni}_{0.2}\text{Zn}_{0.2})\text{O}$, and the 4 cation systems, without Zinc, $(\text{Co}_{0.2}\text{Cu}_{0.2}\text{Mg}_{0.2}\text{Ni}_{0.2})\text{O}$. HEO shows stable capacity retention, while the materials without Zn reveal severe capacity degradation. They also found that removing Zn from the HEO causes a completely different electrochemical behavior during the oxidation of the compound. The CVs and differential capacity plots establish that the absence of Zn leads to a two-step oxidation process rather than a single one. The sample demonstrates that even removing a single element significantly changes the electrochemical properties.

Furthermore, entropy was calculated at 1.39R, which belongs to medium entropy oxides. In the context of configurational entropy calculations, Zn should still be calculated. Zn is one of the compounds in the first discovery of HEO in 2015 refers to

the entropy associated with the arrangement of different cations within a crystal structure. Here are a few reasons why cation Zn (or any other cation) should be considered in configurational entropy calculations:

a) Mixing of Cations: High entropy oxides typically consist of multiple cations, such as Zn, Mn, Co, Ni, and Fe, distributed randomly within the crystal lattice. Cation Zn introduces additional complexity to the system, as its arrangement and interaction with other cations affect the overall configurational entropy. Taking into account the different cations enables a more comprehensive analysis of the disorder within the crystal structure.

b) Disorder and Entropy: Configurational entropy arises from the disorder in the arrangement of cations. Including Zn allows for a more accurate assessment of the disorder in the system, as each cation contributes to the overall configurational entropy based on its position and interaction with neighboring cations. By considering cation Zn, the configurational entropy calculation captures the full extent of disorder in the system, providing a more precise understanding of the material's thermodynamic properties.

c) Thermodynamic Modeling: Including cation Zn in configurational entropy calculations enables more accurate thermodynamic modeling and predictions. Thermodynamic models aim to describe and predict the behavior of materials under different conditions. By accounting for all the relevant cations, including Zn, the models can better capture the phase stability, phase transitions, and other thermodynamic properties of the high entropy oxides or multi-component materials.

d) Material Design and Optimization: High entropy oxides have garnered interest due to their unique properties and potential applications. Understanding the configurational entropy, including the contribution from cation Zn, can aid in designing and optimizing these materials. By considering the complete set of cations, researchers can tailor the composition and arrangement of cations to achieve desired properties, such as enhanced stability, improved catalytic activity, or specific electronic or magnetic behavior.

In summary, considering cation Zn (or other relevant cations) in configurational entropy calculations is important to capture the full extent of disorder and complexity in high

entropy oxides or multi-component materials. It allows for more accurate thermodynamic modelling, provides insights into the material's properties, and supports designing and optimizing these materials for various applications.

4.1.6 Transmission Electron Microscope (TEM)

The elemental analysis of a small section was determined using TEM analysis in Fig. 31. HEO-3 has the smallest, which is 2.95 ± 0.29 nm, and the most difficult-to-measure particle sizes, whereas HEO-6 and HEO-9 have particle sizes that are 23.16 ± 7.56 nm and 90.42 ± 3.27 nm, respectively. Agglomeration caused the particle to grow more prominent as the calcination increased.

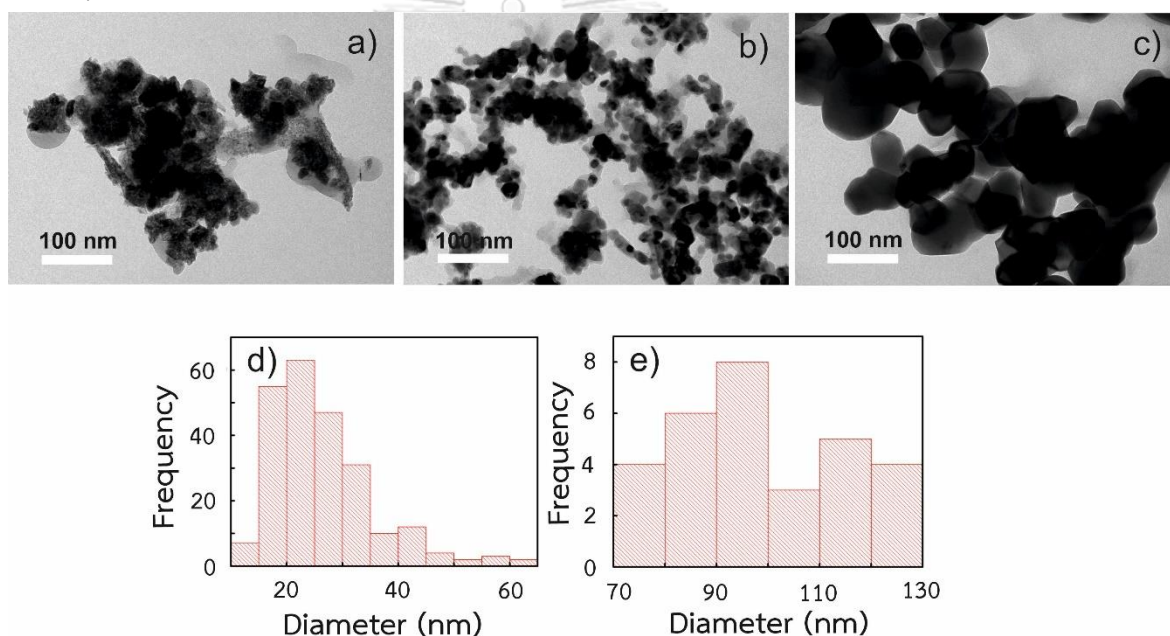


Fig. 31. TEM images of $(\text{FeCoNiMnZn})_3\text{O}_4$ at a) HEO-3, b) HEO-6, and c) HEO-9.

4.1.7 BET Surface area analysis

Through N₂ adsorption-desorption isotherms at 77.00 K, the specific surface areas were determined in Fig. 32. HEO-3, HEO-6, and HEO-9 all have surface areas that have been determined to be 69.59, 16.52, and 3.18 m²g⁻¹, respectively.

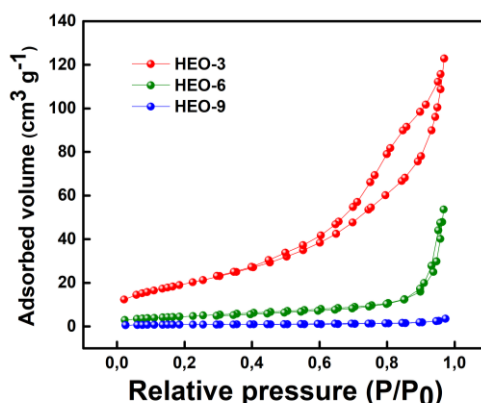


Fig. 32. N₂ adsorption-desorption isotherms of HEO-3, HEO-6, and HEO-9 samples.

In lithium-ion battery applications, a small surface area is more favorable than a large surface area for the electrode materials. Here are the reasons:

- 1) **Stability:** one of the critical challenges in lithium-ion batteries is forming a solid-electrolyte interphase (SEI) layer on the electrode surface. This layer acts as a passivation layer and helps stabilize the electrode-electrolyte interface. A smaller surface area reduces the overall contact area with the electrolyte, leading to a lower SEI growth rate and improved long-term stability.
- 2) **Electrolyte Consumption:** lithium-ion batteries operate through the transport of lithium ions between the electrode materials and the electrolyte. With a smaller surface area, the amount of electrolyte needed for the ion transport is reduced. This can result in lower electrolyte consumption, improved cycling efficiency, and longer battery lifetime.
- 3) **Electrode-Electrolyte Interface:** a larger surface area may initially provide better contact between the electrode and electrolyte, but it can also lead to higher surface and side reactions. These reactions can consume active materials, reduce the battery's coulombic efficiency, and cause capacity fading over time. A smaller surface area mitigates these issues by minimizing unwanted reactions at the electrode-electrolyte interface.
- 4) **Structural Integrity:** high surface area can increase surface strain and structural instability during lithiation and delithiation processes. This can lead to mechanical degradation and reduced cycling stability. A smaller surface area

reduces these strain effects, enhancing the structural integrity of the electrode material.

To conclude, a small surface area is generally preferred over a large one for lithium-ion battery applications to improve stability, minimize side reactions, reduce electrolyte consumption, and enhance cycling performance. There is also important to note that other factors, such as the specific electrode material's composition, particle size, and morphology, also play significant roles in the overall battery performance.

Using nanomaterials is a common method to improve the electrode rate capabilities of LIBs because of the shorter diffusion lengths and greater contact surfaces between the electrode and the electrolyte [7]. Because of their large specific surface area and surface energy, nanoparticles accumulate, which compromises their cyclic stability. HEO, on the other hand, are frequently created by mechanical mixing followed by high-temperature annealing to generate a single solid solution phase, resulting in large particle sizes and reduced capacity retention. High crystallinity has been shown to promote cyclability despite the enormous particle sizes. To optimize the performance of the HEO anode, it is required to adjust the particle size and crystallinity. Furthermore, HEO increased the production of solid-electrolyte interphase layers, which consumed Li irreversibly due to its greater surface areas from smaller particle size.

In the context of high entropy oxides as anode materials in lithium-ion batteries, there is no direct correlation between the surface area and conductivity. While it is generally true that a larger surface area can offer advantages regarding electrode-electrolyte interface, active material utilization, and electron transfer, it does not necessarily guarantee improved conductivity in HEO anode materials. The conductivity of HEO is primarily determined by factors such as their composition, crystal structure, defect concentration, and ionic/electronic transport mechanisms [77]. These factors are more significant in determining the material's conductivity than the surface area alone. In some cases, increasing the surface area of the HEO anode material can lead to higher capacitance or improved electrochemical performance due to increased active material availability and electrode-electrolyte interaction. However,

it does not directly translate into improved conductivity. To summarize, while a larger surface area can have benefits in terms of specific electrochemical processes, it does not directly correlate with improved conductivity in HEO anode materials for lithium-ion batteries. The conductivity of HEOs depends on various intrinsic factors of the material itself.

4.2 Electrochemical performance of $(\text{FeCoNiMnZn})_3\text{O}_4$

4.2.1 Cyclic voltammetry (CV)

The performance of the HEO electrode was measured electrochemically. The reaction voltage, reversibility, and anionic redox reactions are commonly known via cyclic voltammetry (CV) used to examine HEO-3, HEO-6, and HEO-9 samples. CV has the following advantages such as: 1) the chemical process being reversed, 2) identifying oxidation and reduction processes, and 3) altering test parameters such as the scan rate [78]. Fig. 33 depicts the acquired curves in the first five cycles with various anodic and cathodic peaks. All samples showed a prominent oxidation peak at about ~ 1.6 V, caused by the HEO's delithiation (re-conversion) processes. In the subsequent negative scan, CV peaks for HEO-6 and HEO-9 were combined into two peak positions. In other words, as the cycle progressed, the cathodic and anodic curves substantially overlapped, indicating excellent electrochemical reversibility of the $(\text{FeCoNiMnZn})_3\text{O}_4$. Meanwhile, HEO-3 was only around ~ 0.8 V because of its non-single-phase nature and impurity phase. Fig. 34 displays the HEO has been investigated via CV profile recorded 0.1 - 1.0 mV/s. The shapes of CV pictures in $(\text{FeCoNiMnZn})_3\text{O}_4$ can be well retained, even increasing the scan rates, implying exceptional stability as an electrode. The CV of each elemental is displayed in Fig. 35. They are all different peaks due to their components.

In the case of lithium-ion batteries, the anode material is typically the negative electrode. During charging, the anode material undergoes lithium intercalation or incorporation reactions, which change its oxidation state or composition. This process is responsible for storing lithium ions in the anode during charging. Regarding the peak

observed in the CV curve for the anode material [78], it can provide important information:

a. Anodic Peak: The peak appearing during the forward scan represents the oxidation process occurring at the anode. It indicates the release of lithium ions or a change in the composition of the anode material.

b. Peak Potential: The potential at which the peak occurs (voltage on the x-axis) can provide insights into the electrochemical stability and performance of the anode material. It can help determine the voltage range in which the anode material operates efficiently.

c. Peak Shape and Current: The shape and magnitude of the peak can reveal information about the kinetics of the intercalation/incorporation process and the overall performance of the anode material. Broader or asymmetrical peaks could suggest sluggish kinetics or other side reactions.

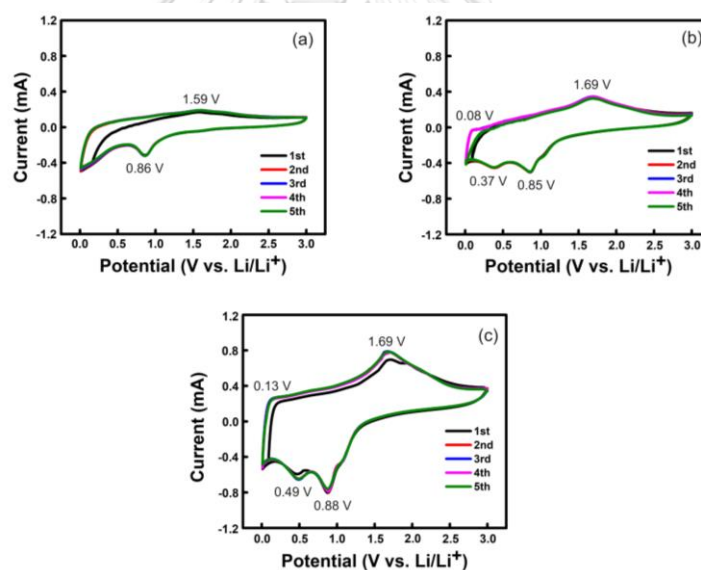


Fig. 33. CV curves for a) HEO-3, b) HEO-6, and c) HEO-9 at 0.1 mVs^{-1} and 0.00 - 3.00 V. In high-entropy oxides, the calcination temperature can impact the material's structural and electrochemical properties, influencing the peaks observed in cyclic voltammetry. Here are some factors that explain why higher calcination temperatures may result in larger peaks:

- 1) Crystallinity and Particle Size: higher calcination temperatures often promote increased crystallinity and larger particle sizes in high-entropy oxides. This

improved crystallinity can lead to better electronic and ionic conductivity within the material, allowing for more efficient charge transfer during the CV measurement. Consequently, the more significant peaks observed in CV can indicate enhanced electrochemical activity and higher specific capacity.

- 2) Enhanced Crystalline Phase Formation: higher calcination temperatures can promote the formation of desired crystalline phases in high-entropy oxides. These crystalline phases may have more favorable electronic and ionic transport properties, improving electrochemical performance. These well-defined crystalline phases can contribute to the larger peaks observed in CV.
- 3) Increased Oxidation State: higher calcination temperatures can also lead to higher oxidation states of the constituent elements in high-entropy oxides. This increase in oxidation state can result in greater charge storage capacity and higher redox activity during the CV measurement, leading to more significant peaks.

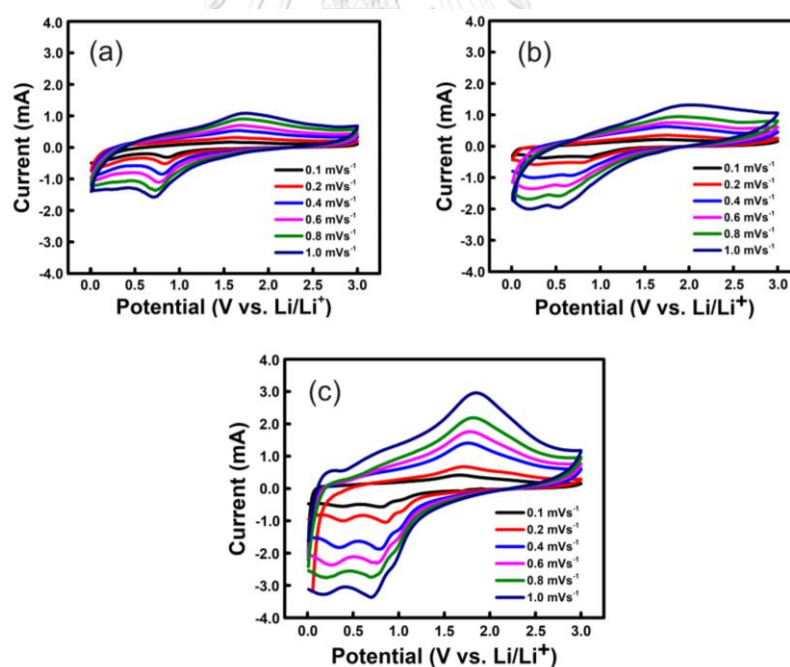


Fig. 34. CV curves of $(\text{FeCoNiMnZn})_3\text{O}_4$ a) HEO-3, b) HEO-6, c) HEO-9 at different scan rates 0.1 - 1.0 mV/s .

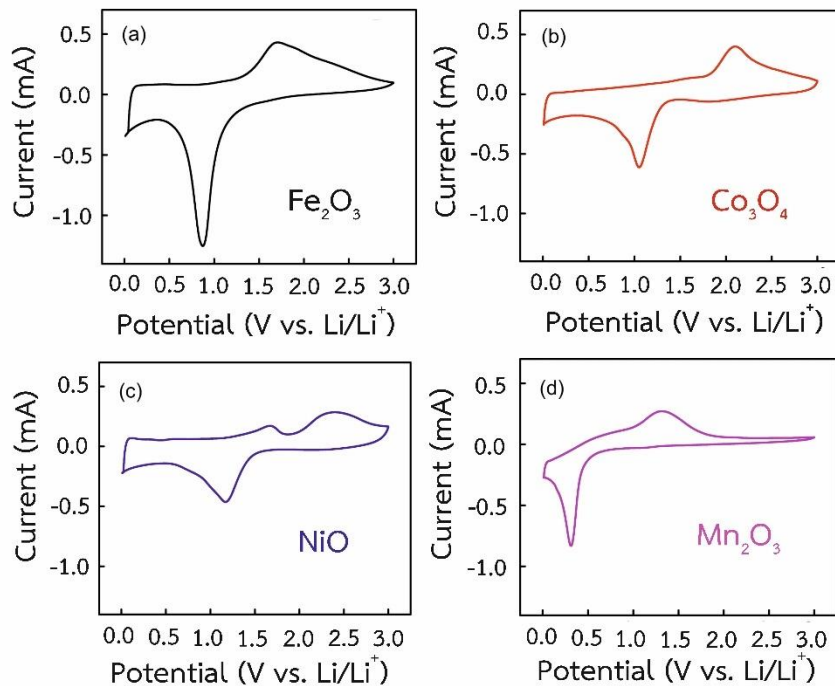


Fig. 35. The initial CV curves for a) Fe, b) Co, c) Ni, and d) Zn oxides at 0.1 mV/s.

4.2.2 Galvanostatic charge-discharge

Expression for specific capacitance (the capability of a material object or device to store electric charge) for galvanostatic charge-discharge curve explains in Fig. 36 below, and it needs the current setting on the instrument as Table 15 when testing the battery.

$$\begin{aligned}
 \Delta Q &= C \cdot \Delta V \\
 C &= \frac{\Delta Q}{\Delta V} \\
 C_p &= \frac{m \Delta V}{\Delta Q} \\
 I &= \frac{\Delta Q}{\Delta t} \\
 \Delta Q &= I \cdot \Delta t \\
 \frac{I}{m} &\rightarrow \text{current density} \rightarrow \text{current per unit mass} \\
 \frac{I}{m} &= Im \\
 C_p &= \frac{Im \Delta t}{\Delta V} \rightarrow \text{Specific Capacitance} \\
 Im &\rightarrow \text{current density} \\
 \Delta t &\rightarrow \text{discharging time} \\
 \Delta V &\rightarrow \text{potential drop}
 \end{aligned}$$

Fig. 36. The formula of specific capacitance.

How to calculate current (I)

Cu foil = 0.0136 gram

Cu foil + coating = 0.0167 gram

Coating = 0.0167 – 0.0136 = 0.0031 gram

=> 0.0031 gr x weight (80%)

=> 0.0031 x 0.8

=> 0.00248 gram

Table 15. The current setting on the instrument.

A/g	A (Setting)	mA
0.05	0.000124	0.124
0.1	0.000248	0.248
0.2	0.000496	0.496
0.5	0.001240	1.240
0.6	0.001488	1.488
0.8	0.001984	1.984
1.0	0.002480	2.480
1.5	0.003720	3.720
2.0	0.004960	4.960
3.0	0.007440	7.440

The first five charge & discharge curves for each element (NiO, Mn₂O₃, Co₃O₄, Fe₂O₃, and various HEO electrodes) are shown in Fig. 37 and are recorded at 100 mA g⁻¹. The specific capacity of Ni, Mn, Co, Fe, HEO-3, HEO-6, and HEO-9 oxides is in Table 16. In charge-discharge measurements of lithium-ion batteries using high-entropy oxides, it is often observed that the specific capacity in cycle 1 is larger than in subsequent cycles (Cycles 2, 3, and so on). This behavior can be attributed to several factors:

- 1) Activation and Formation of SEI: in the first cycle, the high-entropy oxide electrode undergoes activation processes, including forming the solid electrolyte interphase (SEI) layer. The SEI layer forms due to side reactions between the electrode material and the electrolyte, acting as a passivating layer on the electrode surface. During this initial cycle, the SEI layer forms, and

the electrode undergoes changes that can contribute to a larger specific capacity. In subsequent cycles, the activation processes are already initiated, and the SEI layer is typically established, resulting in a reduced additional capacity contribution.

- 2) **Electrode Restructuring and Stabilization:** In the first cycle, the high-entropy oxide electrode may undergo structural rearrangements and restructure due to the lithiation/delithiation process. This can increase surface area and enhance electrochemical activity, producing a larger specific capacity. Subsequent cycles exhibit less restructuring, as the electrode has already undergone some stabilization, leading to a smaller specific capacity.
- 3) **Loss of Active Material or Electrolyte:** high-entropy oxides may experience a loss of active material or electrolyte during the initial cycling. This loss can occur due to mechanical degradation, dissolution, or side reactions. As a result, the available capacity in subsequent cycles may be reduced, leading to smaller specific capacities.
- 4) **Electrolyte Decomposition:** In the initial cycle, the electrolyte can decompose due to the high potential experienced during charging. This decomposition can consume lithium ions and reduce the available capacity for subsequent cycles.
- 5) **Irreversible Side Reactions:** during the first cycle, irreversible side reactions may occur at the electrode-electrolyte interface or within the electrode material. These reactions can lead to the consumption of lithium ions or irreversible changes in the electrode structure, resulting in a larger specific capacity in the first cycle.

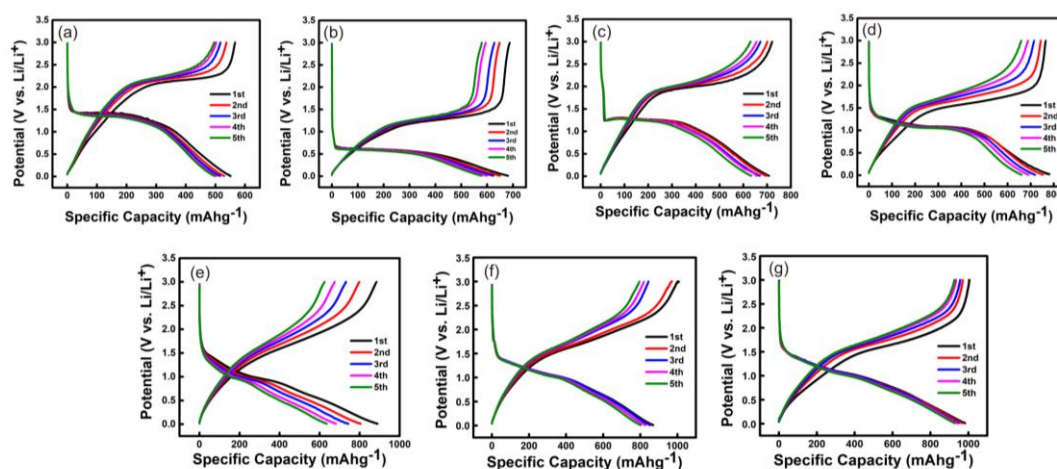


Fig. 37. Initial five charge & discharge curves of a) NiO, b) Mn_2O_3 , c) Co_3O_4 , d) Fe_2O_3 , e) HEO-3, f) HEO-6, and g) HEO-9 electrodes calculated at 100 mA g^{-1} .

Table 16. The specific capacity of Ni, Mn, Co, Fe, HEO-3, HEO-6, and HEO-9 oxides at 100 mA g^{-1} .

Oxide	Cycle 1	Cycle 2	Cycle 3	Cycle 4	Cycle 5
	mAh/g				
NiO	566.2	537.4	517.4	503.4	496.9
Mn_2O_3	686.7	648.2	627.9	594.6	579.5
Co_3O_4	721.2	701.2	671.8	655.8	631.0
Fe_2O_3	764.2	743.3	714.6	687.9	659.6
HEO-3	1090.9	1003.6	938.0	877.2	830.6
HEO-6	1116.6	1059.5	1012.7	976.6	949.4
HEO-9	1146.6	1133.3	1118.3	1101.9	1094.6

The charge-discharge curves of the HEO electrodes at various scan rates ranging from $50\text{-}2000 \text{ mA g}^{-1}$ are in Fig. 38. HEO-3, HEO-6, and HEO-9 have charge capacities, as detailed in Table 17. Except for HEO-3, which supplied 2000 mA g^{-1} , all electrodes produced reversible capacities higher than those of industrially available graphite anodes, demonstrating the HEO's potential for LIBs applications. When compared to HEO and each constituent, HEO-9 has the highest capacity. The electrodes' curve and the CV results are both accurate. HEO-3, HEO-6, and HEO-9 electrodes have first-cycle coulombic efficiency (CE) values of 100.6%, 86.3%, and 97.7%, respectively. The rising

electroactivity of the agglomerated particles may contribute to the high CE of the HEO-3 electrode.

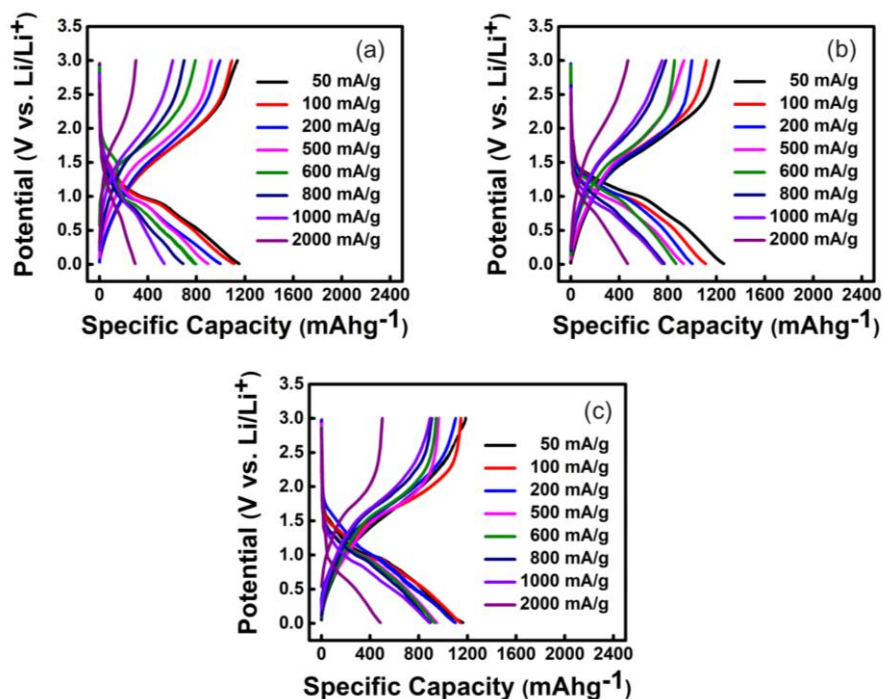


Fig. 38. Charge & discharge curves of the HEO-3, HEO-6, and HEO-9, measured at different specific currents a), b), and c), respectively.

Table 17. The specific capacity of HEO-3, HEO-6, and HEO-9 at different current conditions.

Current (mA)	HEO-3 (mAh/g)	HEO-6 (mAh/g)	HEO-9 (mAh/g)
50	1136.2	1220.3	1333.5
100	1090.9	1116.6	1146.6
200	993.8	998.5	1101.6
500	922.8	932.8	963.8
600	791.2	855.2	943.6
800	698.4	784.4	905.6
1000	604.4	753.2	892.8
2000	300.4	472.0	500.4

In the context of charge-discharge measurements in lithium-ion battery applications, a smaller current can lead to a larger specific capacity for high-entropy oxides. Here are the explanations:

- 1) **Electrode Kinetics:** the kinetics of charge transfer at the electrode/electrolyte interface plays a crucial role in determining the specific capacity of a material. A smaller current is applied during charge-discharge cycles, allowing for more efficient charge-transfer processes.
- 2) **Diffusion Limitations:** in high-entropy oxides, the diffusion of lithium ions within the electrode material can be a limiting factor for achieving high specific capacities. When a smaller current is used, it reduces the concentration gradients and diffusion distances within the electrode material. As a result, lithium ions have more time and opportunity to diffuse into and out of the lattice, enabling higher charge storage and resulting in a larger specific capacity.
- 3) **Electrode Stability:** high-entropy oxides may undergo structural transformations or phase transitions during the charge-discharge process. Operating at lower currents reduces the likelihood of extreme structural changes or phase transitions leading to irreversible capacity loss or electrode degradation. Therefore, a smaller current can help maintain the structural stability of the high-entropy oxide electrode, allowing for better cycling stability and a larger specific capacity over multiple charge-discharge cycles.

While a smaller current may result in a larger specific capacity, there are practical considerations to balance. Using very low currents can significantly increase the charging or discharging time, which may not be feasible in practical battery applications that require rapid energy storage or release. Thus, choosing an optimal current rate should consider the desired balance between specific capacity, cycling stability, and overall battery performance.

4.2.3 Cycling performance, the coulombic efficiencies, and rate capability

The data gathered at a rate of 500 mA g^{-1} were utilized for the cycle stability testing of HEO electrodes, and they are described in Fig. 39a. After 50 cycles, the capacities of the HEO-3, HEO-6, and HEO-9 electrodes were 133, 262, and 579 mAh g^{-1}

¹, respectively with the specific capacity in Table 18. Due to the impurity phase's potential to obstruct Li^+ movement and result in irregularly shaped active material during charge-discharging, the HEO-3 electrode had a low charge-discharge capacity, which may have contributed to the impurity phase's quick capacity fading. HEO-9 electrodes, on the other hand, exhibit outstanding cycle stability that surpasses traditional anodes. Effects of entropy stabilization could support and maintain the reversible transformation during lithiation or delithiation. The long cycles of 50 for each elemental oxide at 100 mA g^{-1} shows in Fig. 39b. In initially, and Iron oxides have the highest capacity; meanwhile, in the end, cobalt oxide is the stable and the highest capacity due to its unique properties as seen in Table 19. Some elementals such as Fe, Co, Ni, and Mn have electrochemical performances except Zinc oxides. ZnO has the limitations, such as its slow chemical reaction kinetics, rapid capacity fading, and poor rate capability, so ZnO must be formed with other materials [79, 80]. There are also performances of 100 cycles at 1.0 A g^{-1} in Fig. 39c, and it is excellent and stable along the charge-discharge and shows the high capacity as in Table 20 at cycles 1, 5, 10, 25, 50, and 100 of HEO-9. The charge-discharge is relatively stable because the curve of different cycles tends to similar or not significant change as in Fig. 39d. The $(\text{FeCoNiMnZn})_3\text{O}_4$ performs significantly better than the previously described HEO, as indicated in Table 21.

The rated capacity from several electrodes is depicted in Fig. 40. The higher rate performance of HEO-9 is attributable to slightly higher O_v concentration than that of the other samples, which enables Li^+ transfer, and higher crystallinity, which also improves capacity and rate capability. HEO-3 and HEO-6, in contrast, have smaller particles than HEO-9. HEO-3 and HEO-6 have large surface areas that make them susceptible to aggregation and reduce cycling stability. This exhibit capacity declines at high charge-discharge rates beginning at 1000 mA g^{-1} . The specific capacity of HEO-3, HEO-6, and HEO-9 at different conditions, each of five cycles, is in Table 22. A high rate capability performance implies that the battery can maintain a significant portion of its specific capacity or energy efficiency even at high current rates. This indicates that the battery can deliver or accept charge rapidly without significantly degrading its performance. On the other hand, poor rate capability performance suggests that the

battery's capacity or efficiency decreases significantly at higher current rates, leading to reduced power output or diminished energy storage capabilities. Batteries with good rate capability can deliver the necessary power quickly, enabling efficient and reliable operation in demanding conditions. Therefore, careful evaluation and characterization of rate capability performance are essential to assess the suitability of a battery for specific high-power applications.

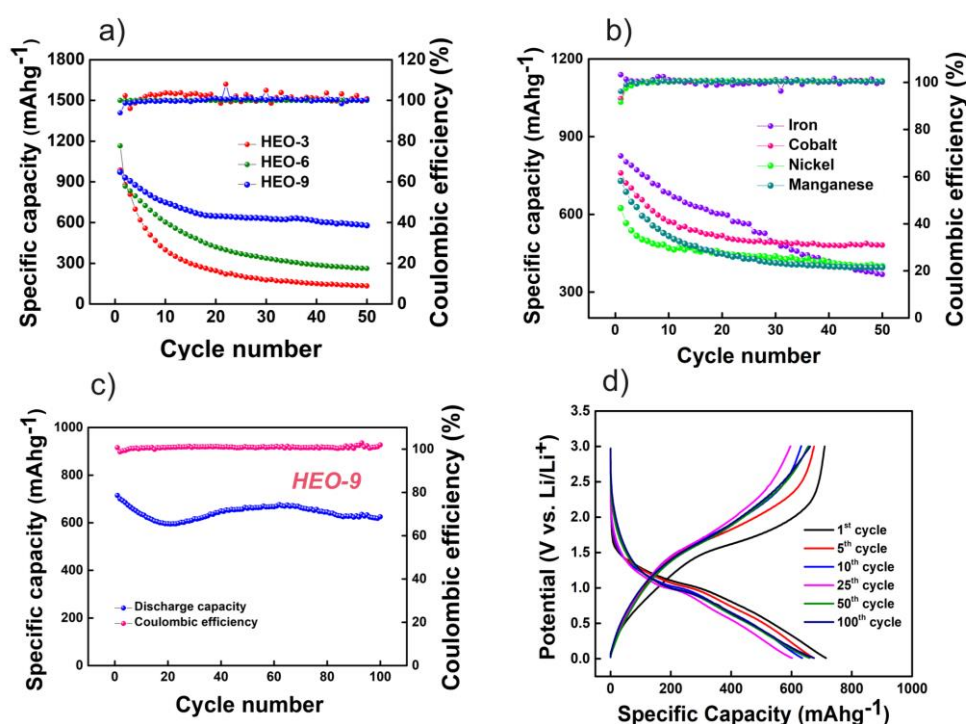


Fig. 39. a) Evaluation of cycling stability of several HEO electrodes at 500 mA g⁻¹ for 50 cycles, b) the performance for 50 cycles of Iron, Cobalt, Nickel, and Zinc oxides at 100 mA/g, c) The performances 100 cycles scan rates at 1.0 A/g, and d) the different cycles of charge-discharge curves at 1000 mA/g of HEO-9.

Table 18. HEO-3, HEO-6, and HEO-9's specific capacity at cycles 1, 10, 30, and 50 at 500 mA g⁻¹.

Oxide	Cycle 1	Cycle 10	Cycle 30	Cycle 50
	mAh/g			
HEO-3	986.8	398.8	177.2	133.2
HEO-6	1164.8	603.2	336.8	261.6
HEO-9	972.4	748.4	631.2	578.8

Table 19. The specific capacity of each elemental oxide at cycles 1, 10, 30, and 50 at 100 mA g⁻¹.

Oxide	Cycle 1	Cycle 10	Cycle 30	Cycle 50
	mAh/g			
Fe ₂ O ₃	825.1	681.7	492.4	368.4
Co ₃ O ₄	759.6	571.6	492.4	481.2
NiO	623.6	469.2	438.0	400.4
Mn ₂ O ₃	728.8	516.0	412.4	395.2

Table 20. The specific capacity of HEO-9 at cycles 1, 5, 10, 25, 50, and 100 at 1.0 A g⁻¹.

Cycle number	HEO-9 (mAh/g)
1	714.7
5	674.0
10	635.6
25	602.0
50	660.4
100	625.5

Table 21. Summary of lithium storage properties of HEO.

Samples	Control variable	Reversible Capacity (cycles)/mAhg ⁻¹	Rate capability/mAhg ⁻¹	Initial discharge/charge capacity (mAhg ⁻¹)	Ref
(Co _{0.2} Cu _{0.2} Mg _{0.2} Ni _{0.2} Zn _{0.2})O	TM-MEO(-Co), TM-MEO(-Cu), TM-MEO(-Zn)	520(50)@0.2 A/g	~270 @1 A/g	980/- @0.05 A/g	[22]
(Mg _{0.2} Co _{0.2} Ni _{0.2} Cu _{0.2} Zn _{0.2})O	Co ₃ O ₄	~900(300)@0.1 A/g	490 @3 A/g	1585/-@0.1 A/g	[4]
(Co _{0.2} Cu _{0.2} Mg _{0.2} Ni _{0.2} Zn _{0.2})O	full-cells with a LiNi _{1/3} Co _{1/3} Mn _{1/3} O ₂ cathode	256(100)@1.6 A/g	~375 @0.16 A/g	446/-@1.6 A/g	[53]
(Ni _{0.2} Co _{0.2} Mg _{0.2} Zn _{0.2} Cu _{0.2})O	Temperature (370, 570, 950°C)	~320(1000)@1 A/g	250 @5A/g	686/- @0.1 A/g	[52]
(FeCoNiCrMn) ₃ O ₄	Temperature (850, 900, 950,	~350(300)@0.5 A/g	182 @ 2A/g	1034/680@0.1 A/g	[3]

	1000°C)				
(FeCoNiCrMn) ₃ O ₄	(FeCoNiCrMn) ₃ O ₄ BM	596.5(1200)@2.0 A/g	~500 @ 2A/g	~1650/1050@0.1 A/g	[51]
(FeCoNiCrMnXLi) ₃ O ₄	(X = Cu, Mg, Zn)	522.1(100)@0.5 A/g	173 @2A/g	1049.9/706@0.05 A/g	[6]
(FeNiCrMnX) ₃ O ₄	(X = Zn, Mg)	386.7(185)@0.5 A/g	~100 @3A/g	~1400/800@0.1 A/g	[8]
(CoNiZnXMnLi) ₃ O ₄	(X = Fe, Cr)	605(100)@0.1 A/g	293 @2A/g	1104.3/-@0.1 A/g	[21]
(FeCoNiMnZn) ₃ O ₄	Each elemental & temperature (300, 600, 900°C)	625.5(100)@1.0 A/g	334.4 @1A/g	1146.64/1140.32@0.1 A/g	This work

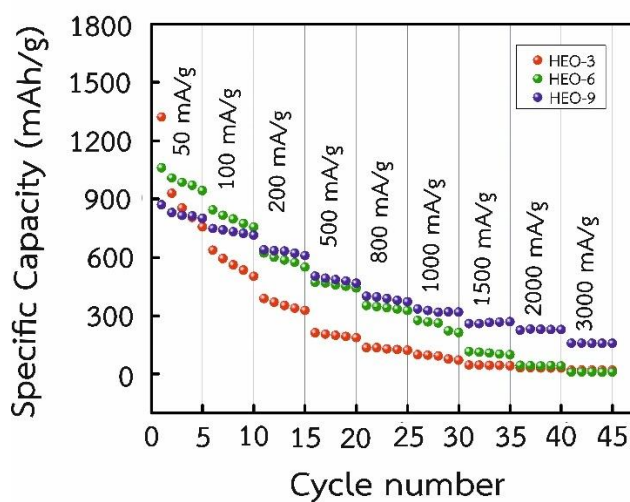


Fig. 40. The ability of different HEO electrodes to compare rates.

Table 22. The specific capacity of HEO-3, HEO-6, and HEO-9 at different conditions.

Current (mA/g)	Cycle	HEO-3	HEO-6	HEO-9
	~mAh/g			
50	1-5	933.2	993.1	826.1
100	6-10	565.8	797.3	731.7
200	11-15	355.3	586.5	627.1
500	16-20	198.9	458.1	485.3
800	21-25	129.4	340.1	387.1
1000	26-30	87.6	248.2	323.5
1500	31-35	44.6	107.4	263.4

2000	36-40	31.3	43.0	228.6
3000	41-45	20.4	10.2	158.1

4.2.4 Electrochemical impedance spectroscopy (EIS)

The acquired spectra at a new electrode are displayed in Fig. 41. About the solid electrolyte interface resistance (R_s), charge-transfer resistance (R_{ct}), and ion diffusion resistance, respectively. The high-frequency patterns in all three samples are semicircles, and the low-frequency patterns are linear. In Table 23, which summarizes the quantitative value, HEO-9 has lower importance than HEO-3 and HEO-6, which improves electronic and ionic conductivity.

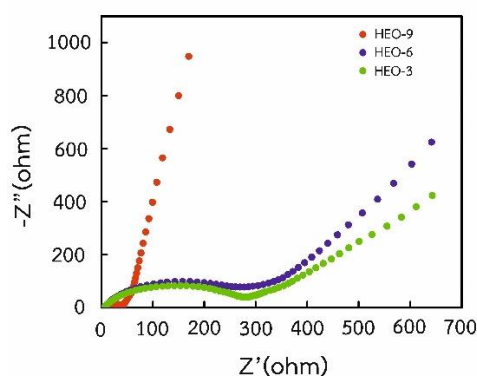


Fig. 41. EIS Nyquist plots of various HEO electrodes.

Table 23. The fitted kinetic parameters of HEO.

Sample	R_{ct} (Ω)
HEO-3	276.1
HEO-6	245.7
HEO-9	46.9

The resistance of Electrochemical Impedance Spectroscopy (EIS) in higher calcination of high-entropy oxides is smaller than in lower calcination. It indicates a lower impedance or resistance to charge transfer processes in the higher calcination state.

Here are the effects:

- 1) Enhanced Electrode-Electrolyte Interface: the calcination process can influence the electrode-electrolyte interface's morphology, composition, and quality. A higher calcination temperature improves interfacial properties, such as increased contact area, reduced interfacial resistance, and improved electronic and ionic conductivity. This results in a smaller resistance observed in EIS measurements, indicating better charge transfer kinetics at the electrode-electrolyte interface.
- 2) Improved Electrode Conductivity: Calcination at higher temperatures can promote better crystallinity and particle connectivity within the high-entropy oxide electrode material. This leads to enhanced electronic conductivity within the electrode, reducing the overall resistance to charge transfer. As a result, the EIS measurement exhibits a smaller resistance value.
- 3) Reduced Electrolyte Decomposition: High-entropy oxides synthesized at higher calcination temperatures often exhibit improved stability and reduced reactivity with the electrolyte. This can mitigate the formation of passivating species or side reactions contributing to higher interfacial resistance. Consequently, the EIS measurement shows a smaller resistance, reflecting improved electrochemical performance.

Therefore, a smaller resistance in EIS measurements at higher calcination should indicate improved charge transfer kinetics and enhanced electrochemical performance in the high-entropy oxide electrode material. HEO with small resistance typically have high conductivity. There are several reasons for this:

- 1) Ionic Conductivity: HEO often exhibit high ionic conductivity, which refers to the ability of ions to move through the material. This is crucial for the transport of lithium ions in lithium-ion batteries. High ionic conductivity is typically associated with low resistance because it allows for efficient ion diffusion and transport, resulting in better overall conductivity [81].
- 2) Defect Structure: HEO can have a defect structure that promotes high conductivity [82]. Defects, such as vacancies or interstitial sites, can act as pathways for ion movement, reducing the resistance in the material. Also,

defects can create more mobile charge carriers, contributing to enhanced conductivity.

- 3) **Composition and Crystal Structure:** The specific composition and crystal structure of HEO can influence their conductivity. Certain elemental combinations and crystal arrangements can facilitate the movement of ions, reducing resistance and promoting high conductivity.
- 4) **Electronic Conductivity:** High electronic conductivity allows for efficient electron transfer, which is crucial for the overall electrochemical performance of the material. Good electronic conductivity contributes to low resistance and high overall conductivity.
- 5) **Microstructure and Grain Boundaries:** The microstructure of HEO, including factors such as grain size and grain boundary characteristics, can impact their conductivity. A well-connected microstructure with fewer grain boundaries can facilitate better ion and electron transport, resulting in lower resistance and higher conductivity.

These properties enable efficient ion and electron transport, enhancing conductivity and reducing HEO resistance.

4.3 After cycling performance of $(\text{FeCoNiMnZn})_3\text{O}_4$

4.3.1 X-ray Diffraction (XRD) after cycling performances

After 50 cycles, it was decided to conduct XRD investigations to look into the crystalline structure. As shown in Fig. 42, the peaks have abruptly increased. The XRD patterns of each element as-synthesized and an electrode examined in Fig. 43. The comparison of after cycling except zinc oxide figured out in Fig. 44. The XRD patterns of high entropy oxides as anodes in lithium-ion batteries can change after 50 cycles due to several factors:

- 1) **Structural Degradation:** the repeated cycling of the battery can induce structural degradation in the high-entropy oxide material. The lithiation and delithiation processes can cause phase transitions, lattice strain, and amorphization of the material. These changes can lead to shifts or broadening

of diffraction peaks in the XRD pattern, indicating alterations in the crystal structure.

- 2) Formation of Lithium-Containing Phases: during cycling, side reactions between the anode material and the electrolyte can form lithium-containing compounds or phases. These compounds may have different crystal structures than the pristine high entropy oxide material. The presence of these additional phases can contribute to the appearance of new diffraction peaks or changes in the intensities of existing peaks in the XRD pattern.
- 3) Electrochemical Decomposition: the cycling process can subject the anode material to electrochemical decomposition, forming new compounds or species. These decomposition products may have different crystal structures than the original high entropy oxide material, leading to observable changes in the XRD pattern.
- 4) Amorphization or Loss of Crystallinity: the repeated lithiation and delithiation processes, mechanical stress, and strain during cycling can induce amorphization or loss of crystallinity in the anode material. Amorphous or poorly crystalline regions do not exhibit distinct diffraction peaks in the XRD pattern, causing a decrease in peak intensity or disappearance of specific peaks.
- 5) Surface Contamination or Oxidation: the exposure of the anode material to the electrolyte and ambient conditions during cycling can lead to surface contamination or oxidation. These surface changes can introduce new phases or alter the surface crystal structure, which can be reflected in the XRD pattern.

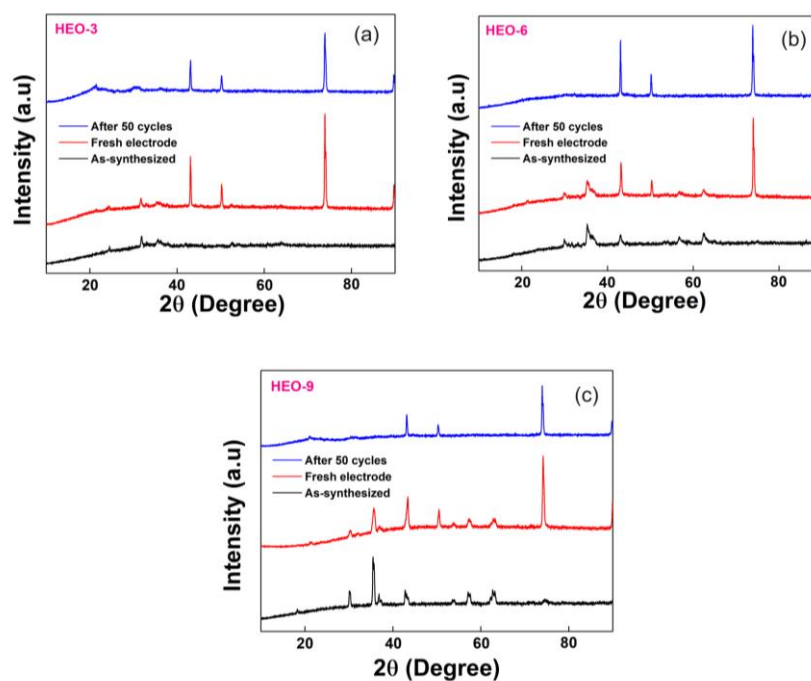


Fig. 42. XRD comparison patterns as-synthesized, electrode and after 50 cycles of a) HEO-3, b) HEO-6, and c) HEO-9.

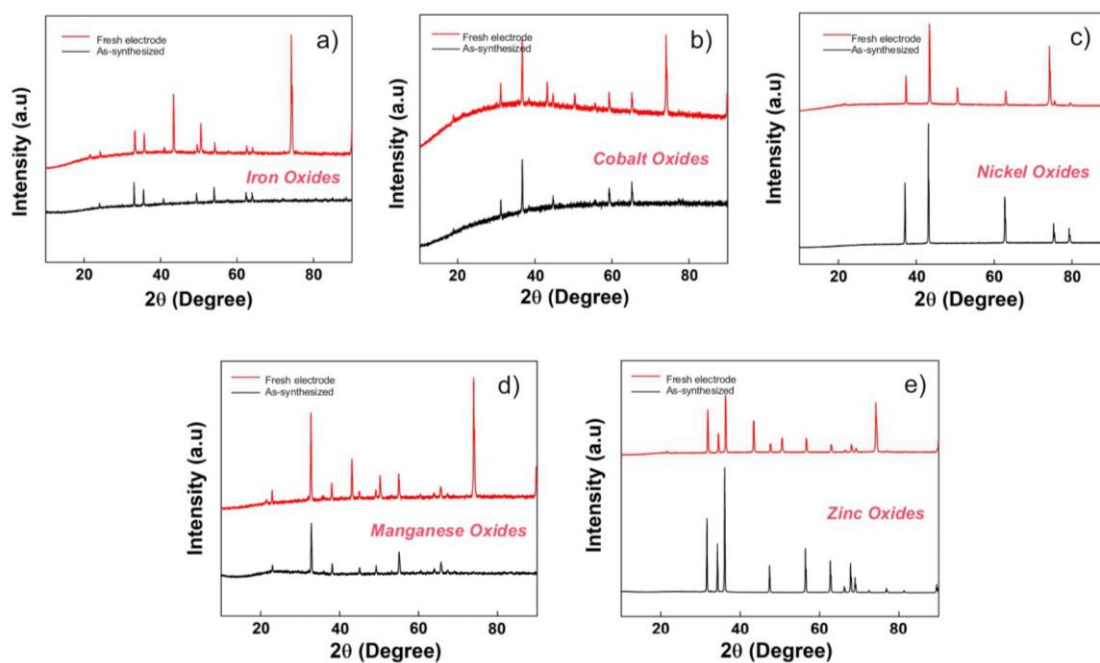


Fig. 43. XRD patterns of comparison as-synthesized and electrode oxides of a) Fe, b) Co, c) Ni, d) Mn, and e) Zn.

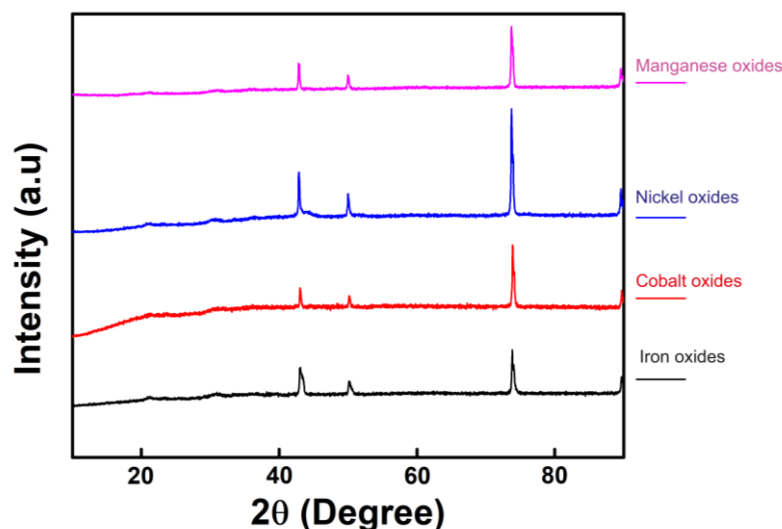


Fig. 44. XRD patterns after 50 cycles of Iron, Cobalt, Nickel, and Manganese oxides.

4.3.2 Scanning Electron Microscope (SEM) and Energy dispersive X-ray spectroscopy (EDS) after cycling performances

The XRD patterns of different charge high entropy oxides synthesized using the hydrothermal method as anodes for lithium-ion batteries can show a phase change to Cu after cycling due to a phenomenon known as "Cu plating" or copper deposition. This occurs when metallic copper (Cu) is formed on the surface of the anode material during battery operation. Several factors can contribute to this phase change:

- 1) Electrochemical Reactions: During lithium-ion battery cycling, the anode material undergoes repeated lithiation and delithiation processes. Under certain conditions, such as high current densities or overcharging, the electrolyte can decompose, reducing copper ions (Cu^{2+}) from the electrolyte onto the anode surface. This results in the formation of metallic copper on the anode material.
- 2) Copper Contamination: In some cases, copper or copper-containing impurities in the electrode materials, electrolyte, or other components of the battery system can also contribute to copper deposition. Even trace copper impurities can initiate and accelerate Cu plating during battery cycling.

The appearance of characteristic diffraction peaks corresponding to copper in the XRD pattern indicates the presence of Cu phases on the anode surface. It is

important to note that copper (Cu) does not typically have a crystal structure commonly observed in XRD patterns. The appearance of distinct copper peaks in the XRD pattern would suggest the presence of metallic copper (Cu) on the surface of the anode due to the copper collector, as discussed previously. However, this is not an intrinsic phase change of the high entropy oxide material but rather a deposition of copper on the surface. Fig. 45a shows discharge to 0.55, 0.40, 0.20, and 0.01 V. The spinel structure of HEO dramatically changed to amorphous and almost dematerialized. Those also happened for charging 1.5, 2.2, and 3.0 V, respectively. The peaks have transformed to increase and alter the phase structure drastically. In addition, the amorphous was maintained after 2 and 50 cycles as well.

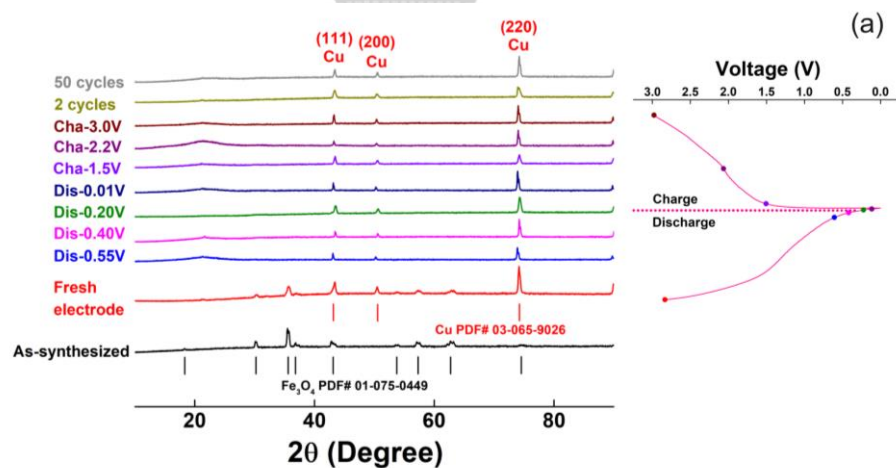
(FeCoNiMnZn)₃O₄ also buffers the volume change; ex-situ SEM is used to compare the volume changes intuitively. The thickness of fresh HEO-3 is 4.2 μm (Fig. 45b), and the electrode layer will extend to 17.1 μm after 50 cycles (Fig. 45e), equating to a 129 % thickness expansion. The thickness of HEO-6 starts at 5.9 μm (Fig. 45c). It increases to 8.1 μm after cycling, a 22 % growth (Fig. 45f). Also, it should be noticed that after cycling, a portion of the spherical active materials is broken. The active material is severely peeled away from the current copper collector. HEO-9, on the other hand, only exhibits a 14 % volume expansion under the same circumstances (from 8.8 to 10.2 μm, Fig. 45d and 45g), keeping its prior spherical form. The findings show that HEO-9 can reduce volume expansion, improving structural stability and producing a robust electrode material. HEO-9 after 50 cycles is described in Table 24 by the elemental percentage of EDS in Fig. 45h.

In the hydrothermal synthesis of high entropy oxides as anodes for lithium-ion batteries, higher calcination temperatures can lead to the formation of small cracks and volume changes after 50 cycles due to several reasons:

- 1) Thermal Stress: higher calcination temperatures can induce thermal stress during synthesis. This stress arises from the differential expansion and contraction of the material as it undergoes heating and cooling. The thermal stress can lead to minor cracks in the material, which can propagate and worsen during cycling.

- 2) Mechanical Stability: higher calcination temperatures can affect the mechanical stability and cohesion of the high-entropy oxide material. Excessive calcination temperatures can lead to grain growth, phase segregation, or reduced sintering, resulting in a less dense and mechanically weaker material. This reduced mechanical stability can make the material susceptible to cracking and volume changes during cycling.
- 3) Electrochemical Reactions: the battery's repeated lithiation and delithiation processes can induce electrochemical reactions within the high-entropy oxide material. These reactions can cause volume changes due to the insertion and extraction of lithium ions into the crystal lattice. If the material is already compromised by small cracks or reduced mechanical stability, the volume changes associated with electrochemical reactions can exacerbate the cracking and lead to further structural degradation.

Optimizing the synthesis conditions, including the calcination temperature, can help minimize the formation of cracks and volume changes, leading to improved mechanical stability and cycling performance in lithium-ion batteries.



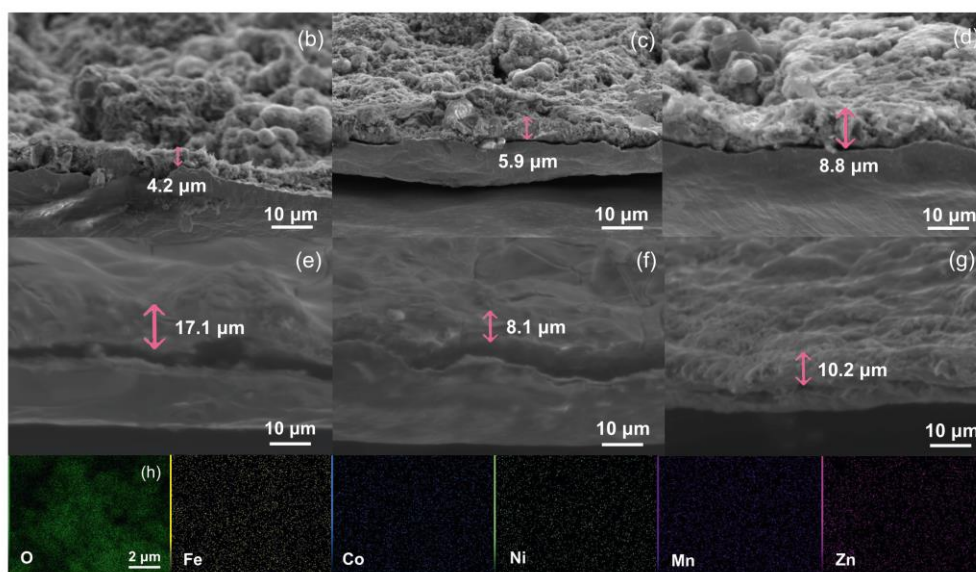


Fig. 45. XRD pattern at different charges a), Morphology characterization of electrodes. Cross-sectional SEM images of the electrode before b) HEO-3, c) HEO-6, d) HEO-9. Cross-sectional SEM images of the electrode after 50 cycles e) HEO-3, f) HEO-6, g) HEO-9. EDS elemental mapping of HEO-9 after 50 charge–discharge cycles h).

Table 24. The elemental concentration of HEO-9 was examined using EDS after 50 cycles.

Element	Series	Atomic (%)
Fe	K-series	33.23
Co	K-series	9.28
Ni	K-series	9.58
Mn	K-series	17.96
Zn	K-series	29.94

The ease of losing composition, specifically for cobalt (Co) and nickel (Ni), in high-entropy oxide (HEO) anode materials for lithium-ion batteries during EDX measurement can be influenced by several factors:

- a) Solubility and Mobility: Co and Ni ions may have a higher solubility or mobility in the electrolyte than other HEO compound elements. This means they are more likely to dissolve into the electrolyte during battery cycling or migrate

within the electrode material [83]. The increased solubility or mobility can result from the specific chemical properties and redox behavior of Co and Ni ions.

- b) Electrochemical Reactivity: Co and Ni ions may undergo more pronounced electrochemical reactions with the electrolyte than other HEO compound elements. These reactions can involve oxidation or reduction processes that result in the dissolution or redistribution of Co and Ni ions. The higher reactivity of Co and Ni can be attributed to their redox activity and potential reactions with the electrolyte components.
- c) Electrolyte Compatibility: The interaction between the electrolyte and the anode material can influence the stability and integrity of the material during cycling. Co and Ni may exhibit lower compatibility with the electrolyte, leading to increased dissolution or surface reactions compared to other elements.
- d) Reduction potential (E_0): An element's reduction potential refers to its tendency to undergo reduction reactions, gaining electrons in the process. Co and Ni have relatively lower reduction potentials [84] compared to other elements commonly used in HEO anode materials, such as iron (Fe), manganese (Mn), and zinc (Zn). This means that Co and Ni ions have a higher propensity to undergo reduction reactions and lose their oxidation states during the battery cycling. In that case, they may preferentially undergo reactions with the lithium ions, resulting in their dissolution into the electrolyte or migration within the anode material. This can lead to a loss of Co and Ni composition, which can be observed during EDX measurement. The higher reducing potential of Co and Ni compared to other elements in the HEO anode material makes them more susceptible to reduction reactions, resulting in their dissolution or redistribution. This correlation with reducing potential contributes to the observed differences in composition during EDX analysis. The overall behavior is a complex interplay of these factors and requires a comprehensive understanding of the material's properties and behavior.

When analyzing a sample using Energy-Dispersive X-ray Spectroscopy (EDX), it is not uncommon to observe variations in the composition of each element. Several factors can contribute to these variations:

- a) **Probe Size and Beam Interaction:** The electron beam used in EDX analysis has a finite probe size. The beam interacts with the sample, and the X-rays are detected to determine the elemental composition. However, the beam size can be larger than the features of interest, resulting in averaging effects. The sample contains regions with different elemental compositions on a smaller scale than the probe size. The measured composition may not accurately represent the local variations.
- b) **Surface Sensitivity:** EDX analysis is surface-sensitive, meaning that it primarily provides information about the surface layers of the sample. There are compositional gradients within the sample, which means the detected X-rays may originate from different depths, leading to variations in the measured composition [85].
- c) **Quantification and Calibration:** EDX analysis requires calibration to convert detected X-ray intensities into elemental concentrations. The calibration process relies on standard samples with known compositions. However, variations in the response factors for different elements or inaccuracies in the calibration process can contribute to compositional discrepancies [86].

To mitigate these factors and improve the accuracy of the EDX analysis: Optimize the analysis conditions, such as beam energy, acquisition time, and detector settings, to minimize artifacts and maximize the sensitivity for the elements of interest. Perform multiple measurements at different locations within the sample to obtain a more representative average composition and assess the level of compositional variation. It is important to note that EDX is a powerful technique but has limitations and requires careful interpretation.

4.3.3 ICP-OES after cycling performances

Regarding the previous result on the elemental composition of EDS measurement, Fe shows the highest atomic percentages, and it is also the same condition when analyzed

by ICP-OES in Table 25. Those are correlated; even though the distribution is not quite similar after the cycling performance of one of them, each elemental still relatively existence. The deviation in the elemental distribution observed after 50 cycling performance of high entropy oxides as anodes in lithium-ion batteries can be attributed to several factors:

- 1) Electrochemical Reactions: during the cycling process of lithium-ion batteries, the anode material undergoes repeated lithiation and delithiation processes, accompanied by electrochemical reactions. These reactions can cause structural changes, phase transitions, and chemical reactions within the high entropy oxide material, leading to alterations in its elemental distribution. Repeated cycling can induce changes in the surface composition and morphology, affecting the atomic ratios of the elements analyzed.
- 2) Mechanical Stress and Strain: cycling-induced mechanical stress and strain can cause deformation and degradation of the high-entropy oxide material. This can result in the formation of cracks, particle fragmentation, or loss of material integrity. These mechanical changes can impact the accessibility of the ICP-OES analysis to different regions of the anode material, leading to variations in the detected elemental distribution.
- 3) Formation of Passivation Layers: during cycling, the high entropy oxide anode material may develop passivation layers or surface films due to reactions with the electrolyte or side reactions. These layers can act as barriers, hindering the diffusion of lithium ions and altering the electrochemical performance. The presence of passivation layers can affect the accessibility of the ICP-OES measurement to different regions of the anode material, resulting in variations in the atomic ratios detected.
- 4) Side Reactions and Impurities: the cycling process can induce side reactions between the anode material and the electrolyte, forming unintended compounds or impurities. These side reactions can alter the composition and distribution of elements within the anode material, leading to differences in the atomic ratios detected by ICP-OES.

Table 25. Elemental distribution of HEO-9 after 50 cycles by ICP-OES measurement.

Element	Atomic (%)
Fe	37.40
Co	12.92
Ni	5.73
Mn	25.58
Zn	18.37

In conclusion, there is the desirable characteristic making a crucial factor in designing and optimization of lithium-ion battery systems [87]:

- 1) *High lithium conductivity* is essential for enabling efficient: a) Ion transport: it ensures rapid and unhindered movement of lithium ions through the electrolyte, facilitating efficient charge and discharge processes; b) Improving rate capability also enables the battery to support high charge and discharge rates by facilitating the fast movement of lithium ions. This is particularly important in applications that require quick charging or high-power output, c) Enhancing cycling stability by reducing the formation of side reactions and improving the efficiency of lithium-ion transport. This contributes to longer cycle life and better capacity retention over time; d) Maintaining electrochemical stability: lithium-ion batteries often operate at high voltages, which can lead to potential reactions or decomposition of the electrolyte if it has low chemical stability. High lithium conductivity allows for efficient ion transport while maintaining the electrochemical stability of the electrolyte, reducing the likelihood of unwanted chemical reactions and electrolyte degradation.
- 2) *Appropriate Electrolyte*: choosing the appropriate electrolyte composition is crucial for coin-cell lithium-ion batteries due to several factors [88]: a) Ionic Conductivity: The electrolyte in a coin-cell lithium-ion battery should have high ionic conductivity to facilitate the movement of lithium ions between the

anode and the cathode. High ionic conductivity ensures efficient charge and discharge processes, enabling better battery performance; b) compatibility with Electrode Materials: The electrolyte must be compatible with the chosen electrode materials, both the anode and cathode. Compatibility ensures that the electrolyte does not chemically react with the electrodes, leading to degradation, passivation, or the formation of undesired solid-electrolyte interphase (SEI) layers. Incompatibility between the electrolyte and electrode materials can adversely affect battery performance and stability; c) Safety: The electrolyte should contribute to the overall safety of the battery. It should have low flammability and resist thermal runaway or hazardous reactions. Selecting a suitable electrolyte composition can help mitigate the risk of battery failures, such as short circuits or thermal events; d) Environmental Considerations: The electrolyte composition may also be chosen, considering environmental considerations. The electrolyte should ideally contain environmentally friendly and sustainable components with minimal ecological impact.

- 3) *Good electron conductor [89]*. For several reasons: a) Electron Transport: In a lithium-ion battery, electrons flow through an external circuit, providing the electrical current that powers devices or systems. Efficient electron transport maximizes the battery's power output and energy efficiency. Good electron conductors enable rapid and unhindered movement of electrons between the battery electrodes, minimizing internal resistance and voltage losses; b) Overall Battery Efficiency: Efficient electron transport reduces energy losses within the battery and maximizes the conversion of chemical energy to electrical energy. When electrons can easily flow through promising conductive pathways, less energy is dissipated as heat, leading to higher overall battery efficiency. Improved efficiency translates to longer battery runtimes and reduced waste of energy during charge and discharge processes; c) Thermal Management:

Efficient electron conductors help with thermal management in lithium-ion batteries. When electrons encounter high resistance or bottlenecks in their flow, it can lead to localized heating and temperature gradients within the battery. Good electron conductors reduce such resistive heating and help maintain uniform temperature distribution, contributing to the battery's safety and longevity.



CHAPTER 5

CONCLUSION

5.1 Conclusion

In this work, we investigated a new High-entropy nanoparticle $(\text{FeCoNiMnZn})_3\text{O}_4$ powder as an anode for lithium-ion batteries. Firstly, it was successfully synthesized using the hydrothermal process and then heated for 6h in the air at various temperatures (HEO-3, HEO-6, and HEO-9) and each basic oxide. Secondly, the electrode has been prepared and tested the physical and chemical characteristics such as XRD, SEM-EDS, TEM, ICP-OES, BET, and XPS. Thirdly, they also investigate the electrochemical performance such as cyclic voltammetry at 0.1 mV/s and different scan rates from 0.01 to 3.00 V, charge-discharge at various rates ranging from 20 to 2000 mA/g and initial five curves at 100 mA/g, cycling stability of various HEO and each elemental electrodes evaluated for 50 cycles and the performances 100 cycles scan rates at 1.0 A/g at HEO-9, comparative rate capability of various HEO electrodes, and impedance measurement. Poor cycle performance is caused by an impurity phase in HEO-3 at the lower calcining temperature.

On the other hand, the single-phase HEO-9 has outstanding cycle performance after 50 charge-discharge cycles due to its high crystallinity and particle sizes, which are associated with stabilizing high entropy and excellent rate capability, resulting in solid electronic conductivity. We also investigate after-cycling performances using XRD, SEM-EDS, and ICP-OES. HEO-9 is the only one that does not have a significant volume change, and the elemental of all HEO electrodes is still distributed well. This study represents a promising new strategy for creating the next generation of lithium-ion batteries electrode materials, particularly in the context of massive energy storage systems.

5.2 Recommendations for future work

The introduction of HEO for energy-storage applications, particularly in batteries, has attracted interest in recent years. HEO has much to offer applicants because of its intriguing structure and capabilities. Conducting a detailed characterization of the

anode material, including complementary techniques such as microscopy and spectroscopy, requires a more comprehensive understanding of the structural changes and degradation mechanisms.



REFERENCES



จุฬาลงกรณ์มหาวิทยาลัย
CHULALONGKORN UNIVERSITY

1. Mair, J., et al., Sizing domestic batteries for load smoothing and peak shaving based on real-world demand data. *Energy and Buildings*, **2021**. 247.
2. Zheng, Y., et al., A Spinel (FeNiCrMnMgAl)₃O₄ High Entropy Oxide as a Cycling Stable Anode Material for Li-Ion Batteries. *Processes*, **2021**. 10(1).
3. Wang, D., et al., Spinel-structured high entropy oxide (FeCoNiCrMn)₃O₄ as anode towards superior lithium storage performance. *Journal of Alloys and Compounds*, **2020**. 844.
4. Qiu, N., et al., A high entropy oxide (Mg_{0.2}Co_{0.2}Ni_{0.2}Cu_{0.2}Zn_{0.2}O) with superior lithium storage performance. *Journal of Alloys and Compounds*, **2019**. 777: p. 767-774.
5. Lokcu, E., C. Toparli, and M. Anik, Electrochemical Performance of (MgCoNiZn)_{1-x}Li_xO High-Entropy Oxides in Lithium-Ion Batteries. *ACS Appl Mater Interfaces*, **2020**. 12(21): p. 23860-23866.
6. Duan, C., et al., New spinel high-entropy oxides (FeCoNiCrMnXLi)₃O₄ (X = Cu, Mg, Zn) as the anode material for lithium-ion batteries. *Ceramics International*, **2021**. 47(22): p. 32025-32032.
7. Nguyen, T.X., et al., Co-free high entropy spinel oxide anode with controlled morphology and crystallinity for outstanding charge/discharge performance in Lithium-ion batteries. *Chemical Engineering Journal*, **2022**. 430.
8. Xiao, B., et al., High entropy oxides (FeNiCrMnX)₃O₄ (X=Zn, Mg) as anode materials for lithium ion batteries. *Ceramics International*, **2021**. 47(24): p. 33972-33977.
9. Chen, H., et al., A new spinel high-entropy oxide (Mg_{0.2}Ti_{0.2}Zn_{0.2}Cu_{0.2}Fe_{0.2})₃O₄ with fast reaction kinetics and excellent stability as an anode material for lithium ion batteries. *RSC Adv*, **2020**. 10(16): p. 9736-9744.
10. Zhao, J., et al., Air-stable and freestanding lithium alloy/graphene foil as an alternative to lithium metal anodes. *Nat Nanotechnol*, **2017**. 12(10): p. 993-999.
11. Zhang, L., H.B. Wu, and X.W.D. Lou, Iron-Oxide-Based Advanced Anode Materials for Lithium-Ion Batteries. *Advanced Energy Materials*, **2014**. 4(4).

12. Xu, X., et al., Micron-sized iron-oxide secondary particles as anode material for high volumetric-energy-density of lithium-ion batteries. *Materials Today Energy*, **2018**. 7: p. 80-86.
13. Xianjun Zhu, Y.Z., Shanthi Murali, Meryl D. Stoller, and Rodney S. Ruoff, Nanostructured Reduced Graphene Oxide/Fe₂O₃ Composite As a High-Performance Anode Material for Lithium Ion Batteries. *ACS Nano*, **2011**.
14. Zhou, G., et al., Graphene-Wrapped Fe₃O₄ Anode Material with Improved Reversible Capacity and Cyclic Stability for Lithium Ion Batteries. *Chemistry of Materials*, **2010**. 22(18): p. 5306-5313.
15. Chengxin Peng, B.C., Yao Qin, Shihe Yang, Chunzhong Li, Yuanhui Zuo, Siyang Liu, and J. Yang, Facile ultrasonic synthesis of CoO Quantum dot/graphene nanosheet composites with high lithium storage capacity. *ACS Nano*, **2012**.
16. Zhou Guangmin, D.-W.W., Li-Chang Yin, Na Li, Feng Li, and Hui-Ming Cheng, Oxygen Bridges between NiO Nanosheets and Graphene for Improvement of Lithium Storage. *ACS Nano*, **2012**.
17. Wang Hailiang, L.-F.C., Yuan Yang, Hernan Sanchez Casalongue, and Y.L. Joshua Tucker Robinson, Yi Cui, and Hongjie Dai, Mn₃O₄-Graphene Hybrid as a High-Capacity Anode Material for Lithium Ion Batteries. *ACS Communications*, **2010**.
18. Guo, C.X., et al., A Hierarchically Nanostructured Composite of MnO₂/Conjugated Polymer/Graphene for High-Performance Lithium Ion Batteries. *Advanced Energy Materials*, **2011**. 1(5): p. 736-741.
19. Kushima, A., et al., Leapfrog cracking and nanoamorphization of ZnO nanowires during in situ electrochemical lithiation. *Nano Lett*, **2011**. 11(11): p. 4535-41.
20. Zhao, J., et al., Entropy Stabilization Effect and Oxygen Vacancies Enabling Spinel Oxide Highly Reversible Lithium-Ion Storage. *ACS Appl Mater Interfaces*, **2021**. 13(49): p. 58674-58681.
21. Tian, K.-H., et al., High-entropy chemistry stabilizing spinel oxide (CoNiZnXMnLi)₃O₄ (X = Fe, Cr) for high-performance anode of Li-ion batteries. *Rare Metals*, **2021**. 41(4): p. 1265-1275.
22. Sarkar, A., et al., High entropy oxides for reversible energy storage. *Nat Commun*, **2018**. 9(1): p. 3400.

23. Garche, J., Encyclopedia of Electrochemical Power Sources. **2009**: Elsevier Science.
24. Pender, J.P., et al., Electrode Degradation in Lithium-Ion Batteries. *ACS Nano*, **2020**. 14(2): p. 1243-1295.
25. Wu, Y., Lithium-ion Batteries, Fundamentals and Applications. **2015**.
26. Mitsunobu Sato, L.L.a.H.N., Lithium-ion batteries – thin film for energy materials and devices. **2020**.
27. Gong, Z. and Y. Yang, Recent advances in the research of polyanion-type cathode materials for Li-ion batteries. *Energy & Environmental Science*, **2011**. 4(9).
28. Liu, G., et al., Three-dimensional hierarchical wreath-like $\text{Co}_3\text{O}_4@ \text{TiO}_2$ as an anode for lithium-ion batteries. *Journal of Alloys and Compounds*, **2019**. 780: p. 948-958.
29. Wen, Z., et al., High rate electrode materials for lithium ion batteries. *Solid State Ionics*, **2008**. 179(27-32): p. 1800-1805.
30. Ji, L., et al., Recent developments in nanostructured anode materials for rechargeable lithium-ion batteries. *Energy & Environmental Science*, **2011**. 4(8).
31. Han, L., et al., Design of Automatic Production Line for Electrode Defects Inspection of Li-Ion Power Battery. *Applied Mechanics and Materials*, **2013**. 470: p. 400-403.
32. Chen, L., et al., Spent lithium-ion battery materials recycling for catalytic pyrolysis or gasification of biomass. *Bioresour Technol*, **2021**. 323: p. 124584.
33. Wei, L., et al., Surface sulfidization of spinel $\text{LiNi}_{0.5}\text{Mn}_{1.5}\text{O}_4$ cathode material for enhanced electrochemical performance in lithium-ion batteries. *Chemical Engineering Journal*, **2020**. 384.
34. Bresser, D., S. Passerini, and B. Scrosati, Leveraging valuable synergies by combining alloying and conversion for lithium-ion anodes. *Energy & Environmental Science*, **2016**. 9(11): p. 3348-3367.
35. Zhu, J., T. Wierzbicki, and W. Li, A review of safety-focused mechanical modeling of commercial lithium-ion batteries. *Journal of Power Sources*, **2018**. 378: p. 153-168.

36. Al-Gabalawy, M., N.S. Hosny, and S.A. Hussien, Lithium-Ion Battery Modeling Including Degradation Based on Single-Particle Approximations. *Batteries*, **2020**. 6(3).
37. Cantor, B., et al., Microstructural development in equiatomic multicomponent alloys. *Materials Science and Engineering: A*, **2004**. 375-377: p. 213-218.
38. Yeh Jien-Wei, S.-K.C., Su-Jien Lin, Jon-Yiew Gan, Tsung-Shune Chin, Tao-Tsung Shun, Chun-Huei Tsau, and Shou-Yi Chang, Nanostructured High-Entropy Alloys with Multiple Principal Elements Novel Alloys Design concepts and outcomes. *Advanced Engineering Materials*, **2004**.
39. Fu, M., et al., High-entropy materials for energy-related applications. *iScience*, **2021**. 24(3): p. 102177.
40. Chen, J., et al., Superior cycle life of TiZrFeMnCrV high entropy alloy for hydrogen storage. *Scripta Materialia*, **2022**. 212.
41. Ma, E. and X. Wu, Tailoring heterogeneities in high-entropy alloys to promote strength-ductility synergy. *Nat Commun*, **2019**. 10(1): p. 5623.
42. Loffler, T., et al., What Makes High-Entropy Alloys Exceptional Electrocatalysts? *Angew Chem Int Ed Engl*, **2021**. 60(52): p. 26894-26903.
43. Hussain, I., et al., High entropy alloys as electrode material for supercapacitors: A review. *Journal of Energy Storage*, **2021**. 44.
44. Xu, X., et al., High-entropy alloy nanoparticles on aligned electronspun carbon nanofibers for supercapacitors. *Journal of Alloys and Compounds*, **2020**. 822.
45. Chen, Y., et al., Opportunities for High-Entropy Materials in Rechargeable Batteries. *ACS Materials Letters*, **2020**. 3(2): p. 160-170.
46. Musicó, B.L., et al., The emergent field of high entropy oxides: Design, prospects, challenges, and opportunities for tailoring material properties. *APL Materials*, **2020**. 8(4).
47. Sarkar, A., B. Breitung, and H. Hahn, High entropy oxides: The role of entropy, enthalpy and synergy. *Scripta Materialia*, **2020**. 187: p. 43-48.
48. Rost, C.M., et al., Entropy-stabilized oxides. *Nat Commun*, **2015**. 6: p. 8485.
49. Bérardan, D., et al., Room temperature lithium superionic conductivity in high entropy oxides. *Journal of Materials Chemistry A*, **2016**. 4(24): p. 9536-9541.

50. Yeh, J.-W., Alloy Design Strategies and Future Trends in High-Entropy Alloys. *Jom*, **2013**. 65(12): p. 1759-1771.
51. Xiao, B., et al., High-entropy oxides as advanced anode materials for long-life lithium-ion Batteries. *Nano Energy*, **2022**. 95.
52. Kheradmandfard, M., et al., Ultrafast green microwave-assisted synthesis of high-entropy oxide nanoparticles for Li-ion battery applications. *Materials Chemistry and Physics*, **2021**. 262.
53. Wang, Q., et al., High entropy oxides as anode material for Li-ion battery applications: A practical approach. *Electrochemistry Communications*, **2019**. 100: p. 121-125.
54. Nguyen, T.X., et al., High entropy spinel oxide nanoparticles for superior lithiation–delithiation performance. *Journal of Materials Chemistry A*, **2020**. 8(36): p. 18963-18973.
55. Wang, C., et al., Novel nano spinel-type high-entropy oxide (HEO) catalyst for hydrogen production using ethanol steam reforming. *Nanoscale*, **2023**. 15(19): p. 8619-8632.
56. Anandkumar, M. and E. Trofimov, Synthesis, properties, and applications of high-entropy oxide ceramics: Current progress and future perspectives. *Journal of Alloys and Compounds*, **2023**. 960.
57. Aamlid, S.S., et al., Understanding the Role of Entropy in High Entropy Oxides. *J Am Chem Soc*, **2023**. 145(11): p. 5991-6006.
58. Han, X., et al., Electrospun single-phase spinel magnetic high entropy oxide nanoparticles via low-temperature ambient annealing. *Nanoscale Adv*, **2023**. 5(11): p. 3075-3083.
59. Liu, Y., et al., Multi-doped ceria-based composite as a promising low-temperature electrolyte with enhanced ionic conductivity for steam electrolysis. *Molecular Systems Design & Engineering*, **2023**.
60. Wang, D., et al., Microwave solvothermal synthesis of Component-Tunable High-Entropy oxides as High-Efficient and stable electrocatalysts for oxygen evolution reaction. *Journal of Colloid and Interface Science*, **2023**. 646: p. 89-97.

61. Xue, T., et al., Development of Quinary Layered Double Hydroxide-Derived High-Entropy Oxides for Toluene Catalytic Removal. *Catalysts*, **2023**. 13(1).
62. Payne, M.H.F.a.D.A., Grain-size effect on structure and phase transformations for barium titanate. *Physical Review B*, **1996**. 54.
63. Herrmann, M., W. Engel, and N. Eisenreich, Thermal expansion, transitions, sensitivities and burning rates of HMX. *Propellants, Explosives, Pyrotechnics*, **1992**. 17(4): p. 190-195.
64. Usharani, N.J., et al., Role of size, alio-/multi-valency and non-stoichiometry in the synthesis of phase-pure high entropy oxide (Co,Cu,Mg,Na,Ni,Zn)O. *Dalton Trans*, **2020**. 49(21): p. 7123-7132.
65. Du, M., et al., Preparation and effect of grain size on the thermal stability, phase transition, mechanical property, and photocatalytic property of pyrochlore (La_{0.2}Nd_{0.2}Sm_{0.2}Gd_{0.2}Y_{0.2})₂Zr₂O₇ high-entropy oxide. *Ceramics International*, **2022**. 48(14): p. 20667-20674.
66. Bayraktar, D.O., et al., Effect of synthesis environment on the electrochemical properties of (FeMnCrCoZn)₃O₄ high-entropy oxides for Li-ion batteries. *International Journal of Energy Research*, **2022**. 46(15): p. 22124-22133.
67. Dong, Q., et al., Rapid Synthesis of High-Entropy Oxide Microparticles. *Small*, **2022**. 18(11): p. e2104761.
68. Yen, J.-Z., Y.-C. Yang, and H.-Y. Tuan, Interface engineering of high entropy Oxide@Polyaniline heterojunction enables highly stable and excellent lithium ion storage performance. *Chemical Engineering Journal*, **2022**. 450.
69. Kinsinger, N.M., et al., Nucleation and Crystal Growth of Nanocrystalline Anatase and Rutile Phase TiO₂ from a Water-Soluble Precursor. *Crystal Growth & Design*, **2010**. 10(12): p. 5254-5261.
70. Oskam, G., Metal oxide nanoparticles: synthesis, characterization and application. *Journal of Sol-Gel Science and Technology*, **2006**. 37(3): p. 161-164.
71. Lal, M.S. and R. Sundara, High Entropy Oxides-A Cost-Effective Catalyst for the Growth of High Yield Carbon Nanotubes and Their Energy Applications. *ACS Appl Mater Interfaces*, **2019**. 11(34): p. 30846-30857.

72. Wei, X.-F., et al., High entropy carbide ceramics from different starting materials. *Journal of the European Ceramic Society*, **2019**. 39(10): p. 2989-2994.
73. Brennecke, T., et al., Imaging the distribution of nutrient elements and the uptake of toxic metals in industrial hemp and white mustard with laser-induced breakdown spectroscopy. *Spectrochimica Acta Part B: Atomic Spectroscopy*, **2023**. 205.
74. Moghadam, K. and D. Beauchemin, Forensic analysis by solid sampling electrothermal vaporization coupled to inductively coupled plasma optical emission spectrometry. *Chem Commun (Camb)*, **2023**. 59(53): p. 8190-8204.
75. Xiao, B., et al., Enhanced Li-Ion Diffusion and Cycling Stability of Ni-Free High-Entropy Spinel Oxide Anodes with High-Concentration Oxygen Vacancies. *ACS Appl Mater Interfaces*, **2023**. 15(2): p. 2792-2803.
76. Pan, Y., et al., High-entropy oxides for catalysis: A diamond in the rough. *Chemical Engineering Journal*, **2023**. 451.
77. Li, G., et al., Developing Cathode Materials for Aqueous Zinc Ion Batteries: Challenges and Practical Prospects. *Advanced Functional Materials*, **2023**.
78. Kim, T., et al., Applications of Voltammetry in Lithium Ion Battery Research. *Journal of Electrochemical Science and Technology*, **2020**. 11(1): p. 14-25.
79. Bui, V.K.H., et al., Review of ZnO Binary and Ternary Composite Anodes for Lithium-Ion Batteries. *Nanomaterials (Basel)*, **2021**. 11(8).
80. Laurenti, M., et al., Zinc oxide nanostructures by chemical vapour deposition as anodes for Li-ion batteries. *Journal of Alloys and Compounds*, **2015**. 640: p. 321-326.
81. Bao, C., et al., 12 μm -Thick Sintered Garnet Ceramic Skeleton Enabling High-Energy-Density Solid-State Lithium Metal Batteries. *Advanced Energy Materials*, **2023**. 13(13).
82. Li, M., et al., Activating surface atoms of high entropy oxides for enhancing oxygen evolution reaction. *Chinese Chemical Letters*, **2023**. 34(3).

83. Lv, Y., et al., Engineering of cobalt-free Ni-rich cathode material by dual-element modification to enable 4.5 V-class high-energy-density lithium-ion batteries. *Chemical Engineering Journal*, **2023**. 455.
84. Comba, P., et al., Redox Potentials of High-Valent Iron-, Cobalt-, and Nickel-Oxido Complexes: Evidence for Exchange Enhanced Reactivity. *Israel Journal of Chemistry*, **2020**. 60(10-11): p. 957-962.
85. Wang, H. and P.K. Chu, Surface Characterization of Biomaterials, in Characterization of Biomaterials. **2013**. p. 105-174.
86. Newbury, D.E. and N.W. Ritchie, Performing elemental microanalysis with high accuracy and high precision by scanning electron microscopy/silicon drift detector energy-dispersive X-ray spectrometry (SEM/SDD-EDS). *J Mater Sci*, **2015**. 50(2): p. 493-518.
87. Gao, X., et al., Designed high-performance lithium-ion battery electrodes using a novel hybrid model-data driven approach. *Energy Storage Materials*, **2021**. 36: p. 435-458.
88. Dai, F. and M. Cai, Best practices in lithium battery cell preparation and evaluation. *Communications Materials*, **2022**. 3(1).
89. Hayakawa, E., et al., Design of active-material/solid-electrolyte composite particles with conductive additives for all-solid-state lithium-ion batteries. *Journal of Power Sources*, **2023**. 555.

VITA

NAME Maha Nur Aida

DATE OF BIRTH 18 April 1996

PLACE OF BIRTH Tulungagung

INSTITUTIONS ATTENDED S.Pd at State University of Malang

HOME ADDRESS RT 002/RW 001 No. 49 Dsn. Tamanan Ds. Sukowiyono
Kec. Karangrejo, Kab. Tulungagung, East Java, Indonesia,
66253

